Aalto University
School of Electrical Engineering
Degree Programme in Bioinformation Technology

Aino Tervo

Noise optimization of multi-layer insulation in liquid-helium cryostat for brain imaging

Master's Thesis
Espoo, October 10, 2016

Supervisor: Prof. Risto Ilmoniemi
Advisor: Koos Zevenhoven, M.Sc. (Tech.)

Aalto University
School of Electrical Engineering
Degree Programme in Bioinformation Technology

ABSTRACT OF
MASTER'S THESIS

Author: Aino Tervo

Title:
Noise optimization of multi-layer insulation in liquid-helium cryostat for brain imaging

Date: October 10, 2016 **Pages:** vii + 54

Major: Bioengineering **Code:** F3013

Supervisor: Prof. Risto Ilmoniemi

Advisor: Koos Zevenhoven, M.Sc. (Tech.)

Superconducting quantum interference devices (SQUIDs) can be used as extremely sensitive magnetic-field detectors. They are widely used in biomedical applications such as ultra-low-field magnetic resonance imaging and magnetoencephalography, providing anatomical or functional information of the human brain. To be operated in a superconducting state, the SQUIDs are immersed into a liquid-helium bath, which is housed by a dewar.

In order to keep the helium liquefied, the dewar needs thermal insulation against heat transfer by thermal radiation. The insulation is usually implemented by placing aluminized layers into the vacuum space of the dewar. These layers reflect the thermal radiation efficiently. However, the aluminized insulation layers cause thermal magnetic noise due to the thermal motion of free electrons within the conductors. This noise can be reduced by breaking the metallic layers into small electrically isolated areas. However, there are currently no detailed studies about the effect of the size of the isolated area or the number of the insulation layers on the noise level.

In this thesis, the methods for calculating the thermal magnetic noise from the patched conducting layers are described. In addition, the boil-off rates are estimated. The simulations revealed the effects of the isolated area and the number of layers on the noise and the boil-off. The results also showed that to reach the desired noise level, the isolated areas should be made very small. Since this might not be practical to manufacture, also other insulation materials should be considered.

Keywords: Ultra-low-field magnetic resonance imaging, magnetoencephalography, liquid-helium dewar, multi-layer insulation, thermal magnetic noise

Language: English

Aalto-yliopisto
Sähkötekniikan korkeakoulu
Bioinformaatioteknologian koulutusohjelma

DIPLOMITYÖN
TIIVISTELMÄ

Tekijä:	Aino Tervo		
Työn nimi:	Aivokuvantamisessa käytettävän nesteheliumsäiliön monikerroseristeen kohinan optimointi		
Päiväys:	10. lokakuuta 2016	**Sivumäärä:**	vii + 54
Pääaine:	Biologinen tekniikka	**Koodi:**	F3013
Valvoja:	Prof. Risto Ilmoniemi		
Ohjaaja:	DI Koos Zevenhoven		

Suprajohtavia kvantti-interferenssilaitteita (*Superconducting quantum interference devices*, SQUIDit) voidaan käyttää erittäin herkkinä magneettikenttäantureina. Niitä käytetään laajalti lääketieteellisissä kuvantamismenetelmissä kuten ultramatalan kentän magneettikuvauksessa ja magnetoenkefalografiassa, jotka tuottavat rakenteellista ja toiminnallista informaatiota ihmisaivoista. Jotta SQUIDeja voidaan käyttää suprajohtavassa tilassa, ne ovat upotettuna neste-heliumsäiliöön.

Jotta helium pysyisi nestemäisenä, säiliö on suojattava lämpösäteilyltä. Tämä eristesuoja toteutetaan yleensä asettamalla nesteheliumsäiliön tyhjiötilaan alumiinikerroksia, jotka heijastavat lämpösäteilyä tehokkaasti. Aluminoiduista eristekerroksista syntyy kuitenkin magneettista lämpökohinaa vapaiden elektronien lämpöliikkeen seurauksena. Tämän magneettisen lämpökohinan tasoa voidaan pienentää rikkomalla yhtenäiset metallipinnat pieniksi sähköisesti eristetyiksi alueiksi. Tällä hetkellä ei kuitenkaan tiedetä tarkasti eristettyjen alueiden pinta-alan ja eristekerrosten määrän vaikutusta kohinatasoon.

Tässä työssä kuvataan menetelmä laikutetun metallikerroksen magneettisen lämpökohinan laskemiseksi. Lisäksi työssä lasketaan arvio heliumin kiehumalle. Simulaatioista kävi ilmi eristetyn alueen pinta-alan ja eristekerrosten lukumäärän vaikutus sekä kohinatasoon että kiehumaan. Tuloksista nähtiin myös, että eristetyt alueet tulisi tehdä hyvin pieniksi, jotta kohina saataisiin halutulle tasolle. Koska tällainen materiaali voi olla haastava valmistaa, myös muita eristemateriaaleja tulisi harkita.

Asiasanat:	Ultramatalan kentän magneettikuvaus, magnetoenkefalografia, nesteheliumsäiliö, monikerroseriste, magneettinen lämpökohina
Kieli:	Englanti

Acknowledgements

First of all, I want to thank prof. Risto Ilmoniemi for the opportunity to work in the MEG–MRI Brain Imaging group. It has been fascinating to get to know a small piece of this challenging field of science and technology. I am also grateful to my advisor Koos Zevenhoven for patient guidance during these years. My time in the lab has been enjoyable thanks to my great colleagues. I especially thank my team member Antti for useful discussions.

I am thankful to my family and friends, who have supported me with thoughts and encouraging words. A special thanks goes to my flatmate Elsi for putting up with me every day and for being such hilarious travel company during many unforgettable trips. The next adventures are calling soon!

Espoo, October 10, 2016

Aino Tervo

Acronyms

BOR	Boil-off rate
CDI	Current-density imaging
dc SQUID	Direct-current SQUID
EEG	Electroencephalography
FRP	Fiberglass reinforced plastic
HTS	High-temperature superconductor
LTS	Low-temperature superconductor
MEG	Magnetoencephalography
MLI	Multi-layer insulation
MR	Magnetic resonance
MRI	Magnetic resonance imaging
MSR	Magnetically shielded room
NCI	Neuronal current imaging
NMR	Nuclear magnetic resonance
rf SQUID	Radio-frequency SQUID
RMS	Root mean square
SQUID	Superconducting quantum-interference device
ULF	Ultra-low field

Contents

Chapter 1

Introduction

Magnetoencephalography (MEG) [1] is becoming an increasingly common tool for studying electrical activity of the brain. In MEG, one measures magnetic signals caused by electric currents in the brain, using sensitive magnetic field sensors around the head. The most sensitive MEG sensors are based on superconducting quantum interference devices (SQUIDs) [2]. Information provided by MEG can be used, for example, for the localization of epileptic foci or presurgical planning of tumor patients [3]. It is evident that these applications need a high localization accuracy. However, the spatial accuracy of MEG is limited by inaccuracies in coregistration of the functional data with anatomical images. In addition, with MEG, brain activity is located by solving a so-called inverse problem, which needs a forward model that contains imprecisions as well.

In contrast, magnetic resonance imaging (MRI) [4, 5] provides excellent spatial resolution. In MRI, one detects nuclear magnetic resonance (NMR) signals from the sample as a response to externally applied magnetic fields. Conventionally, MRI is performed in high fields ($> 1\,\mathrm{T}$), but recently there have been growing interest in carrying out MRI in microtesla fields (1–$200\,\mu\mathrm{T}$) [6, 7]. This ultra-low-field (ULF) MRI can be combined with MEG, and a hybrid MEG–MRI device provides more accurate results, since coregistration issues are eliminated [8, 9]. In addition to improving MEG source localization, ULF MRI itself has many other promising features. It does not compete in signal-to-noise ratio with high-field MRI, but the advantages, such as unique contrast information [10, 11], interesting possibilities in pulse sequences [12–14], reduced costs [6], imaging in presence of metals [15], and open geometry [6] offer high motivation to further develop this branch of MRI technology.

Even though hybrid MEG–MRI devices already exist, all the potential of this approach has not yet been exploited. To take on this task, there is an

ongoing project called BREAKBEN (Breaking the Nonuniqueness Barrier in Electromagnetic Neuroimaging). The principal aim of the project is to make the localization of brain activity more accurate and reliable. To achieve this goal, one task in the project is the development of hardware. One vital part of the system is the dewar which houses the SQUID sensors in a liquid-helium bath. To keep the helium liquefied, the dewar requires highly efficient thermal insulation against heat leak. Typical insulation consists of a vacuum space and a stack of reflective layers called multi-layer insulation (MLI) or superinsulation. However, metallic reflectors cause thermal magnetic noise due to Johnson–Nyquist noise, *i.e.*, thermal agitation of free electrons within the material. This dewar noise may limit the measurements of weak magnetic signals if not taken into consideration. As the BREAKBEN project aims to achieve a much better field sensitivity of SQUID sensors compared to the existing MEG–MRI device at Aalto University, the dewar noise in the current system is too high for the new generation SQUIDs. Therefore, a reduction in thermal magnetic noise level is needed.

The aim of this thesis is to study ways to reduce the dewar noise to an acceptable level. Therefore, this thesis provides a review on studies of the thermal magnetic noise and its reduction presented in literature. In addition, methods for modeling magnetic noise and heat transport in dewars for the purposes of the BREAKBEN project are presented. Based on the calculations using these models, this thesis presents a way to implement the superinsulation in order to reduce the noise to the required level, while still maintaining sufficient thermal insulation.

In Ch. 2, ULF MRI and MEG are discussed in more detail. The same chapter includes also their instrumentation, with a special emphasis on the structure of the liquid-helium dewar. Ch. 3 provides an overview of Johnson–Nyquist noise, the consequential magnetic-field noise, and methods for its reduction. Ch. 4 describes methods for calculating the thermal magnetic noise from superinsulation and for estimating the ability of the insulation to keep the helium liquefied. The results based on these models are presented in Ch. 5.

Chapter 2

SQUID-detected brain imaging

This chapter provides background information about low-frequency electromagnetic brain imaging. First, the basic principles of ULF MRI and MEG are discussed. Then, the discussion extends to two essential parts of the hardware used in both imaging modalities – the extremely sensitive sensors based on superconductivity and the cryostat that keeps the sensors in a superconducting state. In addition, the noise sources in this kind of measurements are described. Finally, the present Aalto MEG–MRI system as well as the previously mentioned BREAKBEN project are described.

2.1 Ultra-low-field magnetic resonance imaging

Magnetic resonance imaging is based on nuclear magnetic resonance of atomic nuclei, typically of hydrogen atoms. When these protons are exposed to an external magnetic field $\vec{B}$, the proton spin magnetization rotates around the axis of the field at Larmor frequency $f_{\mathrm{L}} = \gamma\!\!\!^{-}B$, where $\gamma\!\!\!^{-} = \gamma/(2\pi)$ is the proton gyromagnetic ratio. In ULF MRI, the applied measurement field $\vec{B}_0$ is in the microtesla range, corresponding to the frequencies up to a few kHz.

An applied magnetic field also creates a macroscopic magnetization $\vec{M}$ in the sample. The strength of $\vec{M}$, and thus the signal amplitude, depends on the strength of the applied field. Since B_0 is low in ULF MRI, the sample magnetization is created by using a separate and stronger prepolarization field $\vec{B}_{\mathrm{p}}$. The resulting equilibrium magnetization is

$$\vec{M}_{\mathrm{eq}} = \frac{N\hbar^2\gamma^2}{4k_{\mathrm{B}}T}\vec{B}_{\mathrm{p}}\,, \tag{2.1}$$

where N is the number of protons, $\hbar$ the reduced Planck constant, k_{B} the Boltzmann constant, and T the temperature of the sample.

The macroscopic magnetization can be manipulated by using an excitation field $\vec{B}_1$. This is an oscillating or rotating field that tilts the magnetization away from the equilibrium direction, if the frequency of the pulse is equal to the Larmor frequency of the protons. The tilted magnetization rotates around the z axis at the frequency determined by the z-directional $\vec{B}_0$. The weak oscillating magnetic field caused by the rotating magnetization can be measured using a magnetic-field sensor.

After the excitation pulse, the magnetization starts to relax back to the equilibrium direction, simultaneously causing the signal to decay. This signal decay can be explained by two relaxation processes. First, the longitudinal magnetization increases back to its initial value, and this process is characterized by a time constant T_1. Second, the transverse magnetization decays to zero with a representative relaxation time T_2 given by B_0. Different tissues have distinguishable T_1, T_2, and proton densities. These differences allow us to create a contrast between the tissues by using appropriate pulse sequences.

The spatial encoding of the MRI signals is performed using gradients, *i.e.*, spatially varying magnetic fields. One dimension can be encoded by frequency encoding, in which, for example an x gradient $G_x = \partial B_z/\partial x$ changes the proton Larmor frequency in x direction

$$f_{\mathrm{L}}(x) = \gamma\!\!\!^{-}(B_0 + G_x(x))\,. \tag{2.2}$$

Two- or three-dimensional signal encoding can be done by applying phase-encoding gradients. For example, in the y direction, the phase ϕ of the rotating magnetization varies as

$$\phi(y) = \gamma(B_0 + G_y(y))\Delta t\,, \tag{2.3}$$

where Δt is the duration of the gradient pulse.

ULF MRI can be used in several applications, benefiting from the unique possibilities of imaging in ultra-low fields. In current-density imaging (CDI), one determines the pathways of the current flowing inside the sample. With ULF MRI, full information of the electric current-density can be imaged without rotating the sample [13, 14]. CDI can be used for creating an electrical conductivity map of the sample at low frequencies. It may be possible to image neuronal currents directly by means of ULF MRI. To date, neuronal current imaging (NCI) has been studied by simulations and phantom measurements [16–19]. Temperature mapping using ULF MRI has also been reported [12]. In addition, the enhanced T_1 contrast at ultra-low fields could benefit tumor detection [6].

2.2 Magnetoencephalography

In MEG, one measures the weak magnetic signals arising from neural currents. The field caused by a single neuron is too weak to be detected outside the head, but approximately tens of thousands of adjacent cells firing synchronously can cause a detectable field. The fields can be detected during a resting-state measurement or as a response to an external stimulus, such as visual or auditory stimuli.

From the magnetic-field data gathered by MEG, one can locate the active areas on the cortex by solving a so-called inverse problem. However, the solution is non-unique since there can be source currents in the brain that produce very little magnetic field outside of the head. In addition, noise in the measurement data further hinders the source localization. For solving the inverse problem, there are several source models that can be used in the forward solution. For example, equivalent current dipoles or minimum-norm estimates [20] are often used. The forward model requires an estimate of the conductivity profile of the head, which can be created, for example, by segmenting the anatomical MR image and setting an approximate electrical conductivity value for each head compartment. In addition, *a priori* information, such as assumptions of the location and the orientation of the sources, can assist the inverse problem. Obtained MEG source estimates can be coregistered with an MR image for visualization. The source localization accuracy of present MEG is approximately 1 cm.

MEG is a noninvasive and passive modality. It has a short preparation time compared, for example, to electroencephalography (EEG). MEG has an excellent temporal resolution, approximately 1 ms, which enables capturing fast processes in the brain. MEG can also be combined with ULF MRI, improving the workflow and eliminating the coregistration issues.

In basic research, MEG is used for achieving better understanding the functioning of the brain. One application is brain connectivity analysis, in which one studies how different parts of the brain are linked to each other. In clinical studies, MEG has applications in treatment planning and follow-up of various neurological disorders. More comprehensive discussion about MEG can be found, for example in Refs. [1] and [21].

2.3 Sensors based on superconducting quantum interference devices

Both ULF MRI and MEG need extremely sensitive detectors, since the measured magnetic fields are very weak. Currently, most of the sensors used for these modalities are based on superconducting quantum interference devices (SQUIDs) [2] that convert into a voltage the magnetic flux Φ passing through them. A special characteristic of superconducting material is that it loses electrical resistivity below a critical temperature. One widely used superconductor in SQUIDs is niobium (Nb); its critical temperature is 9.2 K.

A SQUID is a superconducting loop with one (rf SQUID) or two (dc SQUID) weak links called Josephson junctions. In biomedical applications, dc SQUIDs are more common and therefore the kind discussed here. Through the Josephson junctions, bound electron pairs can tunnel without resistivity. This supercurrent, or Josephson current, expresses a periodic behaviour as a function of the magnetic flux through the loop. The period of the flux response is called the magnetic flux quantum $\Phi_0 = h/(2e) \approx 2.07\,\mathrm{fTm}^2$, where h is Planck's constant, e is the elementary charge, and f denotes a factor of 10^{-15} (femto). To ease the measurements, the signal is linearized using a so-called flux-locked loop. Since the amplitudes of the current and voltage in a SQUID loop do not depend on the frequency of the signal, SQUIDs are appropriate for detecting the kind of low-frequency signals needed in biomagnetic measurements.

Because the flux noise of the SQUID increases with inductance, it is beneficial to make the SQUID loop small. To effectively measure the magnetic field, a separate larger pickup loop is used. This loop and an input coil form a superconducting flux transformer, which, as the names indicate, picks up the measurable magnetic field resulting in a current flow in the flux transformer circuit and then, the input coil transforms the current into magnetic flux. This flux is further coupled to the SQUID loop via mutual inductance M between the input coil and the SQUID loop. A schematic drawing of a simple SQUID sensor involving a flux transformer circuit and a dc SQUID is shown in Fig. 2.1a. In this figure, the pickup loop forms a magnetometer. A magnetometer is simply a loop which measures the field itself. The magnetic flux through the magnetometer is

$$\Phi = \int_S \vec{B} \cdot d\vec{S} = \int_S B_\perp dS \ , \tag{2.4}$$

which is a surface integral of the magnetic field $\vec{B}$ over the surface enclosed by the loop.

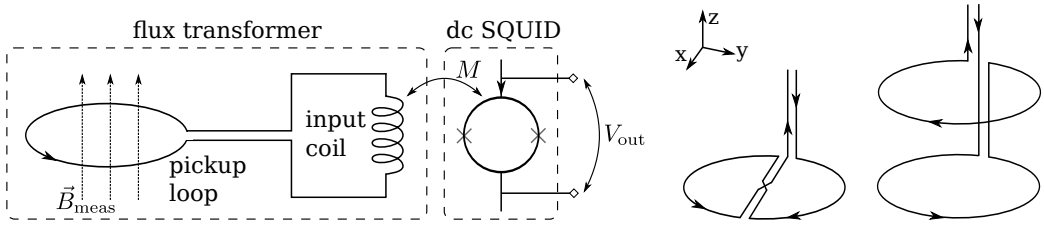

Figure 2.1: (a) A schematic drawing of a SQUID sensor measuring the magnetic field $\vec{B}_{\text{meas}}$. Crosses in the dc SQUID depict Josephson junctions. The pickup coil is a magnetometer type and measures the z component of the field. (b) A first-order planar gradiometer that measures, in this case, the variation of the z component of the field in the y direction. (c) A first-order axial gradiometer which measures the change of B_z in the z direction.

Another common type of a pickup loop is a gradiometer, which measures the spatial difference of the field. First-order planar and first-order axial gradiometers are presented in Figs. 2.1b and 2.1c, respectively. The net flux in the first-order gradiometer can be determined by calculating the fluxes through both of the loops given by Eq. (2.4) and subtracting them from each other. Higher-order gradiometers can be implemented by adding loops to the pick-up coil.

In MEG, a few hundred pickup loops are compiled in a helmet-shaped sensor array in order to get enough coverage around the head to capture brain activity and locate signals with sufficient accuracy. To ensure the performance of these kinds of multi-channel systems, one needs to optimize the sensor type, number of sensors and sensor density [22]. It is especially important to minimize cross-talk between the sensors [23].

Helmet-shaped sensor arrays are also used in ULF-MRI devices intended for brain imaging. In ULF MRI, the sensors need to tolerate relatively high magnetic-field pulses and be able to measure weak fields quickly after them. Therefore, the SQUID sensor is accompanied with a so-called flux dam [24], which is a series of Josephson junctions in the flux transformer circuit. It prevents the induction of too large currents and thus flux trapping in the superconducting structures of the SQUID, but allows current flow when the signal acquisition is done, *i.e.*, when the field change is small. The SQUID itself can be shielded against the direct field pulses by enclosing it in a superconducting shield [6, 25]. After a pulse, it is desirable to restore the SQUIDs to their working state within a few milliseconds in order not to lose

too much NMR signal. Fast recovery can be assisted with a digital detection system [26].

2.4 Cryostats

To function in a superconducting state, SQUIDs need to be cooled below their critical temperature. Typically, the cooling is performed by immersing the sensors in cryogenic, *i.e.*, a low-temperature liquid. If the ULF-MRI prepolarizing magnet is superconducting, it also needs to be put into a cryogenic liquid bath. For low-temperature superconductors (LTS), the liquid used is helium-4 isotope with a boiling point of 4.2 K. There are also high-temperature superconductors (HTS) that could be operated in liquid nitrogen at 77.3 K, but I concentrate on helium systems since we use LTS SQUIDs in our system for MEG and ULF MRI.

The container in which the cryogenic liquid is held is called a cryostat or a dewar. The former refers to a system that maintains cryogenic liquid stable. The latter term comes from James Dewar who was a key contributor to the early steps of dewar development in the late 19^{th} century [27]. A typical bath cryostat is like a vacuum flask, in which a cylindrical vessel is placed inside another. A commonly used helium vessel material is stainless steel due to its mechanical strength, low thermal contraction, and relatively low thermal conductivity [28]. However, in SQUID-based systems, stainless steel cannot be used since, being an electrical conductor, it causes a high level of magnetic noise, as will be discussed later. The best substitute materials for stainless steel are a certain types of fiberglass, for example, fiberglass reinforced plastic (FRP) [2].

Helium has a very low heat of vaporization (2.6 kJ/l), which means that a relatively small amount of heat is sufficient to evaporate one liter of liquid helium. Therefore, a good thermal insulation is needed for reducing the heat flow from the parts of the cryostat at room temperature to the helium vessel, and for keeping the expensive helium liquefied. In order to understand the requirements for effective insulation, let us first study the basic mechanisms of heat transfer.

2.4.1 Modes of heat transfer

According to the second law of thermodynamics, heat flows from a warmer body to a cooler one. Heat can be exchanged within or between bodies by three fundamental modes of heat transfer: conduction, convection, and radiation [29, 30]. Conductive heat transfer occurs within the material itself.

Adjacent particles within the material interact, resulting in energy transfer from the particles having more energy to the less energetic ones. In gases and liquids, conductive heat transfer is due to collisions and diffusion of molecules. In solids, drifting free electrons and vibrating molecules or material structures are responsible for conductive heat transfer. One-dimensional conductive heat flux, *i.e.*, heat transfer per unit time within a homogeneous body between its end plates at temperatures T_{H} and T_{L} can be expressed as

$$\dot{Q}_{\mathrm{cond}} = \frac{kA\left(T_{\mathrm{H}} - T_{\mathrm{L}}\right)}{d} \ , \tag{2.5}$$

where k is the thermal conductivity of the material, A the area of the cross-section of the body, and d the distance between the end plates.

Convection is heat transfer via fluid motion. A typical example of convective heat transfer is a cooling or heating of a solid body using convection. Diffusion or advection moves the fluid relative to the surface of a solid body where heat is exchanged between the fluid and the body. A formula for describing the kind of convective heat transfer is

$$\dot{Q}_{\mathrm{conv}} = hA\left(T_{\mathrm{H}} - T_{\mathrm{L}}\right) \ , \tag{2.6}$$

where h is an experimentally obtained convection coefficient depending on the velocity and viscosity of the fluid as well as the properties of the solid material. A is the contact area of the solid body and the fluid, and T_{H} and T_{L} are the temperatures of the bulk fluid and the solid body, depending on which of them is warmer and which one cooler.

The third mode of heat transfer is thermal radiation, occurring between bodies that are apart from each other. Thermal radiation is generated by collisions of atoms or molecules within the material leading to acceleration of charges or oscillation of dipoles. Thermal radiation is eletromagnetic radiation. In the electromagnetic spectrum (see Fig. 2.2), thermal radiation extends from infrared, through visible light and to the long-wave end of ultraviolet radiation. Its wavelength ranges between 0.1 µm and 100 µm, corresponding to frequencies from $3 \times 10^{12} to 3 \times 10^{15}$ Hz. In helium cryostats, the temperatures of interest are between the liquid-helium temperature and room temperature approximately 300 K. Since the corresponding wavelengths and frequencies lie in the infrared range, infrared radiation is used as a synonym for thermal radiation in cryogenic applications.

Radiative heat transfer is often described using so-called black-body radiation. A black body is an idealized surface that absorbs all the incident radiation and emits radiation with power given by the Stefan–Boltzmann law as

$$P_{\mathrm{emit}} = \sigma_{\mathrm{SB}} A T^4 \ , \tag{2.7}$$

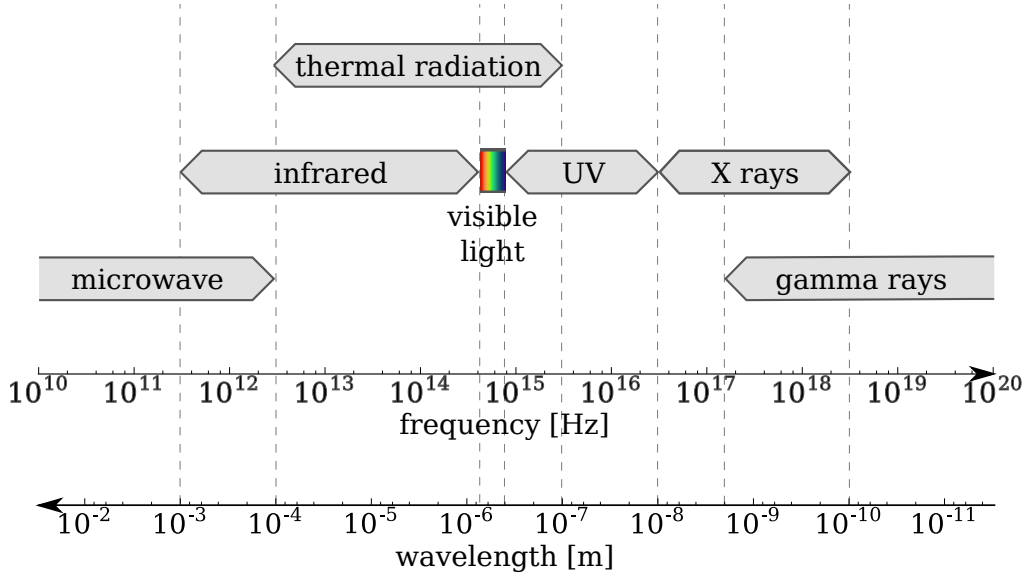

Figure 2.2: Electromagnetic radiation spectrum between 10^{10} Hz and 10^{20} Hz.

where σ_{SB} is the Stefan–Boltzmann constant, A is the surface area, and T the temperature of the black-body emitter. However, a real body is not a perfect absorber or emitter, but radiates only a proportion of the black-body radiation. Therefore, Eq. (2.7) is multiplied by a coefficient called emissivity ε ($0 \leq \varepsilon \leq 1$). The emissivity describes how well the real body is able to radiate heat energy compared to the black body at the same temperature. The emissivity depends, *e.g.*, on the temperature of the body, wavelength and angle of the emitted radiation, material purity and surface roughness. For simplicity, the emissivity values for real surfaces are often averaged over all wavelengths and incident angles, resulting in a value that is called total hemispherical emissivity or average emissivity. Another often used and tabulated value is the emissivity measured normal to the radiating surface.

The net radiative heat transfer between warm and cool real bodies depends on the emissivity of the warm body and heat absorption ability of the cool body, and is given by

$$\dot{Q}_{\mathrm{rad}} = \sigma_{\mathrm{SB}} E F \left(T_{\mathrm{H}}^4 - T_{\mathrm{L}}^4 \right) \ . \tag{2.8}$$

Here, E is a factor combining the emissivity and absorptivity of the bodies and F is a so-called geometrical view factor. Both factors depend on the shape and relative position of the bodies. Examples of calculation of these factors can be found for example in Refs. [27], [29], or [31].

2.4.2 Thermal insulation methods

In cryostats, the main mechanisms of heat inflow to be considered are heat conduction down the inner vessel and the electronic cables, conduction and convection in gas between the inner and outer vessels, and radiation between vessel walls [28, 32]. Conductive heat leak via supporting materials and cables is difficult to avoid but it can be reduced by making the supporting structures long enough, by choosing materials with low thermal conductivity and by designing the electronics carefully. Fortunately, also the boiled vapor can cool off the supporting materials and thus intercept the heat conduction.

Heat transfer from the outer vessel at room temperature to the liquid-helium vessel by gas conduction and convection can be minimized by making a good vacuum (below 10^{-3} Pa) between the vessels. This kind of double-walled vacuum flask was first presented by D'Arsonval in 1887 [33]. If the vacuum space is filled with low thermal conducting powder- [34] or solid foam-insulation [27], the requirements for the vacuum are lower.

Since radiative heat can propagate also in vacuum, special techniques are needed to reduce the radiative heat leak into the helium reservoir. In 1892, J. Dewar showed that silvering the walls of the vacuum space reduces radiative heat leak significantly [27]. The mechanism is based on the fact that silver efficiently reflects thermal radiation. The reflectivity r is the fraction of the incident radiation that reflects back from the body surface. The rest of the incident radiation is absorbed by the material or transmitted through it. The parameters describing these fractions are called absorptivity α and transmissivity τ. However, most of the materials used in cryogenics are opaque to thermal radiation, meaning that their transmissivity is 0 and all the incident radiation is either reflected or absorbed by the material. Insulating materials are often considered as so-called gray bodies, which implies that their radiant properties are approximately independent of the wavelength of the incident radiation when in infrared region.

The emissivity, needed for calculating heat transfer between two bodies [see Eq. (2.8)], relates to these parameters by Kirchhoff's law of thermal radiation, stating that absorptivity and emissivity are equal in thermodynamic equilibrium. This law can also be used as an approximation when the surface and the source are not at the same temperature, requiring that the temperature difference is a few hundred kelvin at most [29]. In liquid-helium dewars, the temperature differences are less than approximately 300 K, and one can write $\varepsilon = \alpha = 1 - r$. Thus, to reflect a large proportion of thermal radiation, one needs to utilize materials with high reflectivity and low emissivity or absorptivity values.

Electrically good conductors are inherently the best reflectors and have

very low emissivity values in the infrared range. However, the surface of the conductor has to be polished, since for instance oxidization, roughening, and contamination of the surface may increase the emissivity significantly. In addition, decreasing the temperature of an electrical conductor reduces its emissivity. The most common electrical conductors used as radiant barriers are pure metals such as silver, copper, gold, and aluminum. However, aluminum is the most practical one since it is inexpensive, light, and does not tarnish as easily as silver or copper.

J. Dewar silvered only the walls of the vacuum space of the cryostat. In the 1950s, it was reported that adding many layers of reflecting material into the vacuum space reduces the radiative heat leak and thus the boil-off [28, 35]. This method is called multi-layer insulation (MLI) or superinsulation. MLI can be implemented simply by using commercial aluminum foil. One needs to add low-thermal-conductive spacers, such as polyester or fiberglass mat or nylon net, between the aluminum layers to reduce heat conduction [28]. The heat conduction between the MLI sheets can also be reduced by crinkling it, reducing the contact area between the adjacent layers [7]. It is worth noting that the efficiency of the MLI is also dependent on the distance between the layers. If too tightly packed, conduction between the reflecting layers dominate [32]. Another MLI solution is to use polyester films, such as Mylar®, aluminized either on one or both sides with a thin layer of aluminum [36].

In the 1960s, it was discovered that adding a cooled shield between MLI layers can further reduce the heat leak. The effect is based on the fact that a proportion of the heat absorbed by the shield is emitted from the inner surface of the shield and the rest is conducted to a cooling system. The radiated heat power depends on the fourth power of the temperature difference between the objects. Thus, adding a refrigerated surface between the helium and room temperature will result in a significant reduction in the radiative heat leak. For example, if one cooled shield is set at 150 K, the radiative heat flux is decreased by a factor of 16 compared to the situation with no cooled shield. A desirable property of the cooled shield is a high thermal conductivity in the direction of the dewar axis. Cooled shields are often made of copper or aluminum due to their good thermal conductivity. Cooling of the shield can be performed actively with a separate refrigeration system, and the refrigeration power can be minimized by careful design of the system [37, 38]. Alternatively, evaporated helium gas can also passively keep the shield cool if the shield is attached to the wall of the helium vessel. Then, the height at which the shield is mounted needs to be optimized [39], and the shield needs to be in good thermal contact with the vessel wall in order to get the shield to work efficiently [2]. To enhance the thermal contact

between the helium gas and the wall, one can force the gas to flow along the vessel walls by placing a foam plug in the upper part of the inner vessel [2].

Radiative heat can also be intercepted by placing a liquid-nitrogen jacket around the helium vessel [27]. Almost all the heat radiated from the room temperature wall is absorbed by nitrogen, leading to boil-off of nitrogen liquid which is inexpensive and has higher heat of vaporization compared to helium. On the other hand, nitrogen shielding requires some additional maintenance due to the nitrogen refilling.

In SQUID systems, the magnetic signal coming from outside the dewar is measured. Since the signal strength decreases with distance, the gap from the sensors to the sample should be as small as possible, which means that there is a trade-off between the sensor–sample distance and efficient insulation. With the current dewar technology, a gap size of approximately 1–2 cm is feasible.

With the above methods, one can make an effective insulation for a liquid-helium dewar. Boil-off of less than 1% of the total volume per day is reachable [28]. However, the boil-off rate (BOR) is usually higher in measurement dewars due to noise requirements and the need of electronic cabling into the dewar. In such a situation, an operation time of one week and a BOR of 15% can be achieved [2]. Methods for calculating heat flux and boil-off rate with a combination of MLI and a cooled thermal shield will be discussed in more detail in Sec. 4.1.

2.4.3 Typical design of a liquid-helium dewar

A simple but typical design of a helium bath cryostat intended for SQUID measurements is depicted schematically by Fig. 2.3. In addition to the parts mentioned earlier, there are also other components essential for practical functioning of the dewar.

The dewar has a valve through which the helium vessel can be cooled and refilled using a specially designed helium transfer siphon connecting the helium storage tank and the helium vessel. For boil-off gas, there is a gas vent-off and evaporation line for directing the helium gas out of the laboratory. Another option is to collect the boiled gas and reliquefy it. The sensors are mounted on an insert to keep them stable and at known position. The vacuum is pumped through an evacuation valve. In the vacuum space, there is often an adsorber trap, typically a charcoal getter, to remove possible residual gas.

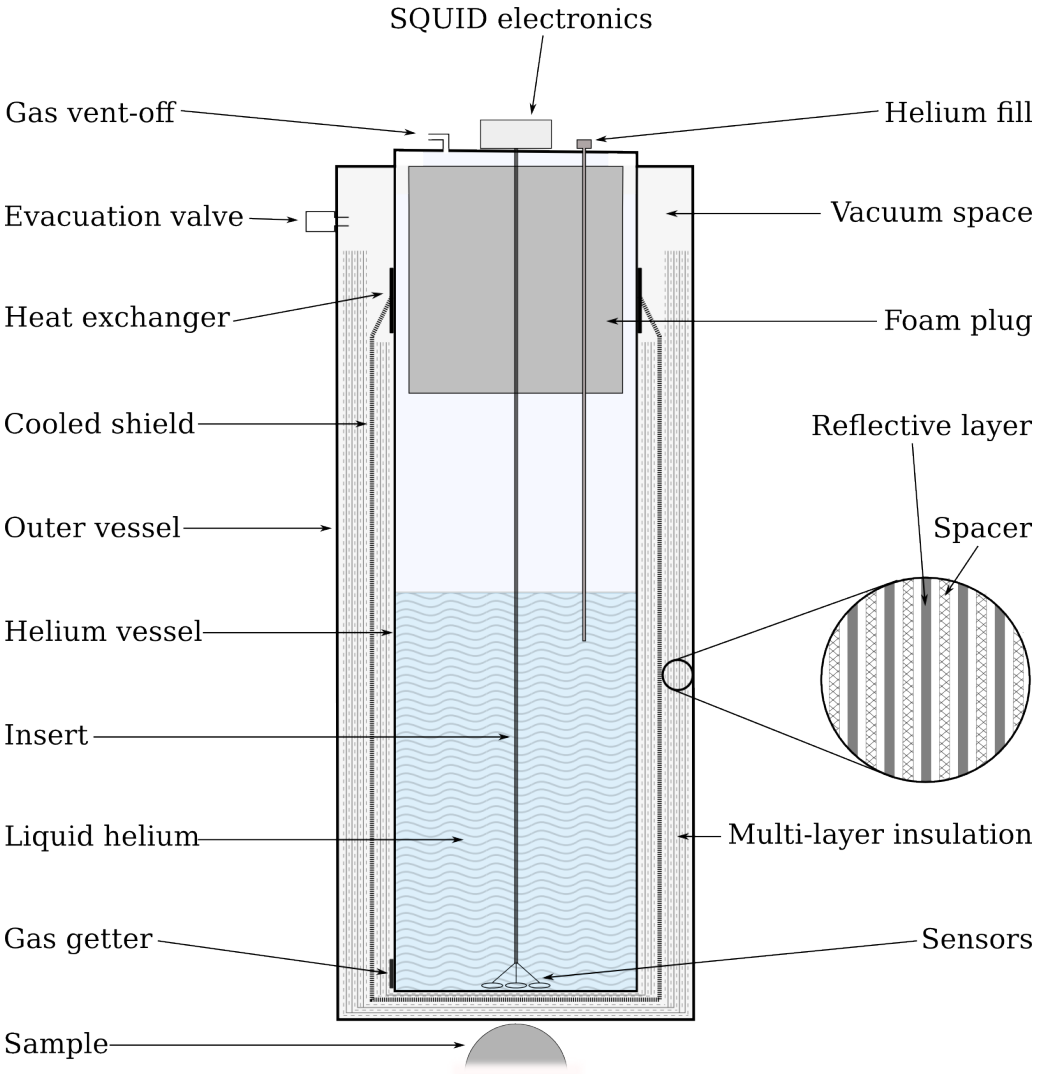

Figure 2.3: A schematic illustration of a typical design of a liquid-helium dewar.

2.5 Noise sources

In MEG and ULF-MRI devices, there are many possible sources of noise that may interfere with the weak signals to be measured. Some of the noise sources are always present while others can be mitigated with special techniques. Before going into details about these noise sources, let us first introduce a few definitions related to noise.

Noise is often expressed in terms of power. The noise power is distributed over the frequency spectrum of the signal. If the noise is distributed equally between all frequencies, it is called white noise. If the noise is inversely proportional to frequency, it is referred to as flicker or $1/f$ noise. The unit of the power spectral density S is W/Hz, which can be thought of as noise power per unit bandwidth. When the signal is measured as a voltage, its noise power spectral density S_V is in units of V^2/Hz. However, the noise can also be scaled to the voltage of the signal by taking the square root, resulting in amplitude spectral density $S_V^{1/2}$ with units of $\mathrm{V}/\sqrt{\mathrm{Hz}}$. Similarly, noise current can be expressed in units of $\mathrm{A}/\sqrt{\mathrm{Hz}}$, flux noise with $\Phi/\sqrt{\mathrm{Hz}}$ and magnetic field noise as $\mathrm{T}/\sqrt{\mathrm{Hz}}$.

In SQUID-based systems, the noise is often divided into system noise and external noise. A portion of the system noise is explained as intrinsic flux noise in the SQUID itself. The white flux noise level is typically around $1\,\mu\Phi_0/\sqrt{\mathrm{Hz}}$, and it is mainly due to thermal fluctuation of charge carriers in a shunt resistor added to avoid hysteresis in the SQUID [2]. The $1/f$ flux noise at low frequencies is caused by fluctuation of critical current and flux trapping lines in the superconductor [2]. The flux noise can be reduced by lowering the temperature and inductance of the SQUID. When measuring magnetic fields, it is also convenient to convert flux noise into field noise of the sensor, which dictates the minimum detectable field. Using Eq. (2.4), the field noise can be determined as $S_{B_\mathrm{n}}^{1/2} = S_{\Phi_\mathrm{n}}^{1/2}/A$, where A is the area enclosed by the pickup loop. This relation indicates that the field noise can be reduced by increasing the area of the pickup loop. In a typical sensor consisting of a flux transformer and a SQUID loop, the field noise is approximately $1\,\mathrm{fT}/\sqrt{\mathrm{Hz}}$ [6].

Another type of system noise is caused by thermal magnetic fields that couple to the sensors limiting the measurements. These noise fields are generated by thermal noise currents in electrically conducting parts of the system which are close to the sensors. One major source of this kind of noise is often the thermal insulation of the liquid-helium dewar, since the multi-layer insulation and the refrigerated shield are typically constructed using metallic materials. The level of dewar noise in typical MEG systems is less than

$3\,\mathrm{fT}/\sqrt{\mathrm{Hz}}$ [40]. Thermal magnetic noise, and especially dewar noise and its reduction methods will be discussed in more detail in Ch. 3. Additional possible sources of thermal magnetic noise are MRI coils. They are usually made of copper wire, which, being a good electrical conductor, may generate a high level of thermal magnetic noise if too close to the sensors. Since the noise is dependent on the wire diameter squared, excessively thick wires should be avoided [6].

In addition to thermal magnetic noise, ULF-MRI coils may cause other issues. Relatively high currents are fed into the coils in order to generate the magnetic fields used in ULF MRI. These ramped currents should be as free of noise as possible so that they do not deteriorate the measurements. Low-noise currents can be produced using a special-purpose low-noise amplifier [41]. Another issue when pulsing relatively high magnetic fields is that they induce eddy currents into conducting parts of the system. The induced eddy currents, in turn, cause secondary fields that may interfere with the measurement if not taken into consideration. These secondary fields can be reduced, for example, by using a self-shielded coil [42] or a DynaCan cancellation waveform generated by an additional coil [43].

Also external noise may disturb SQUID measurements. Typical causes for external noise disturbances are Earth's magnetic field, traffic, and power lines. Their effects can be suppressed by a magnetically shielded room (MSR), which is typically made of aluminum and mu-metal layers. However, the MSR needs careful design, since it is also a source of thermal magnetic noise [44] and eddy-current interference. In a noisy environment, the use of gradiometers is advantageous since they do not detect uniform fields and thus noise from very distant sources. In addition, signal processing can be used for filtering and further reducing the noise.

Interestingly, also the sample or patient may cause some noise. Patient noise is mainly thermal magnetic noise from thermal currents in tissues with an estimated amplitude spectral density of $0.1\,\mathrm{fT}/\sqrt{\mathrm{Hz}}$ at a 5-mm distance from the human body [45].

2.6 Aalto hybrid MEG–MRI system

The hybrid system at Aalto University (see Fig. 2.4a), combining MEG and ULF MRI [9], uses parts from a whole-head MEG device of Elekta Oy (Helsinki, Finland). The dewar bottom is helmet-shaped and the vessels are made out of FRP. The volume of the helium vessel is approximately 90 liters and its hold time is one week. The distance between the sensors and the sample is approximately 1.7 cm. The MRI coils are positioned around the

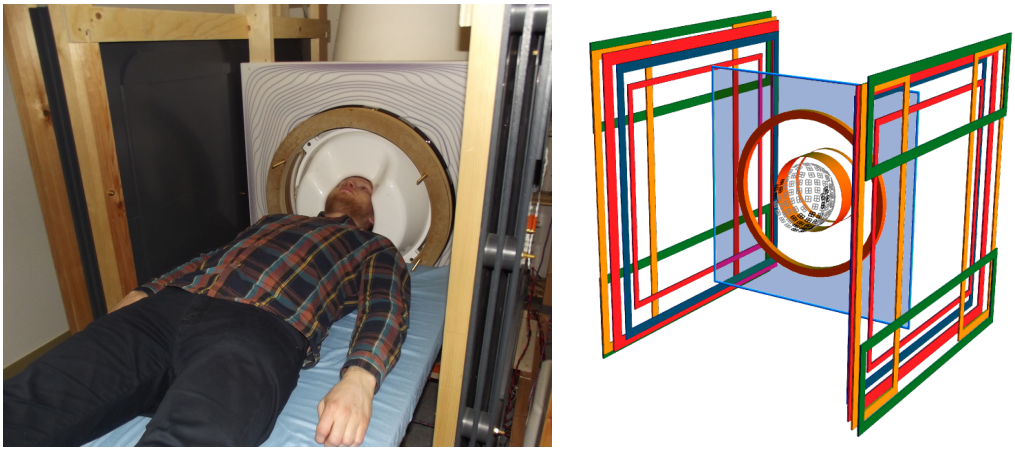

(a) (b)

Figure 2.4: (a) A photograph of the MEG–MRI system at Aalto University. (b) The MRI coil configuration. The prepolarization coil consists of the orange cylinder coils in the middle. The excitation coil is placed on the blue surface, and the measurement field is generated by four rectangular coils shown as red. The x-, y-, and z-gradients are colored yellow, green and blue, respectively.

dewar, except for the prepolarization coil, which is placed in the helium bath. The coil configuration is presented in Fig. 2.4b.

The sensor array of the MEG–MRI system consists of 16 sensor modules on the bottom of the helmet. Each planar module comprises one magnetometer, two orthogonal planar gradiometers and the SQUIDs [25]. Some of the pickup loops are made of 6-µm Nb strips while the others from a lead (Pb) wire with a diameter of 0.5 mm.

The total noise levels of the sensors at the frequency range of 0.1–3 kHz are 4–5 $\mathrm{fT}/\sqrt{\mathrm{Hz}}$ for the magnetometers and 2–4 $\mathrm{fT/cm}/\sqrt{\mathrm{Hz}}$ for the gradiometers. The intrinsic noise levels are 2–4 $\mathrm{fT}/\sqrt{\mathrm{Hz}}$ and 1–3 $\mathrm{fT/cm}/\sqrt{\mathrm{Hz}}$ for the magnetometers and gradiometers, respectively. The rest of the noise is assumed to arise mainly from the thermal radiation shields.

The dewar and the coils are placed inside an MSR with inner dimensions of 4.11, 2.76, and 3.11 m. The MSR consists of two layers of 8-mm aluminum and another two layers of 1-mm mu-metal shells.

2.7 BREAKBEN project

As mentioned in Ch. 1, improving the accuracy of the brain-activity localization is in high demand. To respond to this challenge, there is an ongoing three-year project called BREAKBEN (Breaking the Nonuniqueness Barrier in Electromagnetic Neuroimaging). In the project, there are partners from Aalto University (Finland), Elekta Oy (Finland), Helsinki University Hospital (HUS, Finland), Ilmenau University of Technology (TUIL, Germany), Physikalisch-Technische Bundesanstalt (PTB, Germany), Technical Research Centre of Finland (VTT), and University of Chieti-Pescara (UdA, Italy). The aims of the project and the methods to reach the aims are discussed next.

2.7.1 Aims of the project

The BREAKBEN project has several ambitious aims. As the name indicates, one of the principal aims is to solve the nonuniqueness problem of MEG and EEG. Another goal is to make a breakthrough in neuronal current imaging using ULF MRI. This would give unique source current estimates since MRI locates the signal directly to the origin of the activity – without an ill-posed inverse problem. In addition, current-density imaging will be tested using phantoms and *in vivo*. Furthermore, the aim is to study the impact of these improvements on brain connectivity analysis. All of these aims mentioned need improvements in hardware and software. Therefore, there will be essential improvements, *e.g.*, in sensor, MRI coil and amplifier technology.

The breakthroughs in NCI and CDI will require better ULF-MRI systems both at Aalto University and PTB. The ULF-MRI system at Aalto will be improved by constructing a new hybrid MEG–MRI device. The strength of the prepolarization field will be increased up to 150–200 mT. This build-up of field strength leads to enhancement in power signal-to-noise ratio by a factor of approximately 10000 compared to the first brain images presented in Ref. [9]. In addition, new sensors with a lower noise level are needed. The targeted noise level is below 0.5 $\mathrm{fT}/\sqrt{\mathrm{Hz}}$, but it may be possible to reduce the level even down to 0.1 $\mathrm{fT}/\sqrt{\mathrm{Hz}}$. This reduction corresponds to a ten-fold enhancement in field sensitivity compared to the present systems. Since the prepolarization field strength will be increased, the sensors need to be able to tolerate larger pulses than before and still recover sufficiently fast after the pulse. However, improvements in the sensor technology are useless unless the other noise sources are weaker than the sensor noise level. As discussed previously, one limiting noise source is thermal magnetic noise arising from

the thermal insulation of the measurement dewar. Therefore, a low-noise dewar will be constructed.

The nonuniqueness problem will be approached by combining ULF MRI and MEG into a hybrid device, enabling the measurement of structural and functional information in the same session. This way, one can eliminate coregistration errors and make the source localization more accurate. In addition, accurate conductivity information obtained by CDI would ameliorate the inverse solution in MEG but also in EEG. In addition, NCI data can be used as *a priori* information for the inverse problem. By combining all necessary information, the inverse solution may become unique.

The improved and developed devices and methods will be validated using sophisticated test imaging objects, known as phantoms. Suitable phantoms for NCI, CDI, and conductivity mapping will be constructed. The brain structures and properties such as anisotropic electrical conductivity of the white matter and the shape and conductivity of the skull will be mimicked to the best of one's ability. Moreover, measurements with healthy subjects and patients will be done in order to verify the enhanced ULF-MRI performance as well as the NCI, CDI and brain connectivity protocols *in vivo*.

2.7.2 Requirements for the new ultra-low-noise dewar

As mentioned previously, one requirement is to reduce the dewar noise level below the noise level of the new sensors. And, if possible, the noise level should be reduced to about 0.1 $\mathrm{fT}/\sqrt{\mathrm{Hz}}$, which is the ultimate limit dictated by the thermal noise arising from the patient itself as discussed in Sec. 2.5. By reducing the dewar noise to this value, one ensures that the dewar noise is not the dominant noise source. While reducing the thermal noise level, one needs to take into account the performance of the thermal insulation as well. The boil-off rate should be as low as possible and the refill time as long as possible.

Other important factors to consider are the materials and safety. The construction materials need to be suitable for the MEG and ULF-MRI measurements. For instance, ferromagnetic materials should be avoided in the vicinity of the sensors, since they may cause excessive amounts of noise. However, the system can contain some amount of non-magnetic metals if they do not limit the measurements by for example increasing the thermal noise or induced eddy currents. Thermal contraction of the materials should be on a negligible level or taken into account in the design. Also, materials must be suitable for making a helmet-shaped geometry in the dewar bottom. The main safety aspects involve consideration of helium hazards and a sudden pressure increase.

To start with, a small test dewar will be constructed in order to test the new SQUIDs and also superinsulation. The test dewar will be a flat-bottomed cylinder with a size such that a few sensors fit on the bottom and possibly a small-sized polarization coil. The distance between the sample and the sensors should be made as small as possible. Based on the experience gained with the test system, a helmet-shaped dewar will be constructed with a full sensor array.

Chapter 3

Thermal magnetic noise

As explained in Sec. 2.5, thermal magnetic noise can be a dominant noise source when measuring weak magnetic fields. This chapter begins with a discussion of thermal motion in general and the thermal motion of charge carriers within a conductor. Then, the study is extended to thermal magnetic noise, and especially to the noise present in liquid-helium dewars.

3.1 Thermal motion

Particles in material move randomly due to their thermal energy. The movement of molecules, atoms, electrons or other subatomic particles can be translational, rotational or vibrational. The degrees of freedom of different types of movements depend on the particle structure and its environment.

According to the equipartition theorem, each degree of freedom, *i.e.*, an independent mode of the system, corresponds to an energy of $k_{\mathrm{B}}T/2$. The total internal energy of the system is a sum of the average energies in each independent mode. The internal energy of the system increases with temperature.

Thermal motion is closely related to the fluctuation–dissipation theorem. It states that there is a fluctuation phenomenon associated with the dissipation of energy so that the fluctuation is determined by the dissipation and vice versa. Examples of this kind of pairs are, for example, Brownian motion and drag force as well as Johnson–Nyquist noise and resistance.

3.2 Johnson–Nyquist noise

The thermal motion of the charge carriers in conducting materials cause fluctuations of electric current and potential in the conductor. This process

can be thought of as an electrical analogy of Brownian motion. In conducting liquids, the moving particles are ions, whereas in metals, the charge carriers are free electrons that move stochastically within the atomic lattice. This electrical fluctuation is often called Johnson–Nyquist noise (also Johnson noise, Nyquist noise or thermal noise), of which Johnson published the first experimental observations in the late 1920s [46, 47]. He measured current over various conductors with a vacuum tube and a thermocouple ammeter. He observed that the ratio of the mean-square voltage and resistance $\langle V^2 \rangle / R$ does not depend on the conductor material or shape, but it depends on the temperature of the conductor.

Briefly after Johnson's experimental results, Nyquist gave a theoretical explanation for these observations using statistical mechanics and thermodynamics [48]. He formed the well known Nyquist formula, which states that the spectral density of the thermal noise voltage over a conductor is

$$S_V = 4\, k_\mathrm{B} T R \,, \tag{3.1}$$

where k_B is the Boltzmann constant, T is the absolute temperature of the conductor, and R is the resistance. If we consider Johnson–Nyquist noise over a certain bandwidth Δf, the root-mean-square (RMS) noise voltage is

$$S_V^{1/2} = \sqrt{4 k_\mathrm{B} T R \Delta f} \,. \tag{3.2}$$

A resistor having thermal noise is often represented with a normal resistor symbol in a circuit as seen in Fig. 3.1a. The equivalent circuit for this noisy resistor is a noiseless resistor in a series with a Thévenin voltage source (see Fig. 3.1b). The amplitude of the voltage source is given by Eq. (3.2). One can also make an equivalent circuit with a noiseless resistor and a parallel Norton current source (see Fig. 3.1c). The RMS noise current is then

$$S_I^{1/2} = \frac{S_V^{1/2}}{R} = \sqrt{\frac{4 k_\mathrm{B} T \Delta f}{R}} \,, \tag{3.3}$$

and the spectral density of the noise current

$$S_I = \frac{4\, k_\mathrm{B} T \Delta f}{R} \,. \tag{3.4}$$

To get an idea about the scale of the noise voltage and current, let us consider a 5 Ω resistor at a temperature $T = 293$ K. If the bandwidth is $\Delta f = 1$ kHz, we get $S_V^{1/2} = 8.99$ nV and $S_I^{1/2} = 1.80$ nA, calculated using Eqs. (3.2) and (3.3), respectively.

Eqs. (3.1) and (3.4) indicate that the noise spectral density is frequency independent, so the noise is white. This is the case when the component is

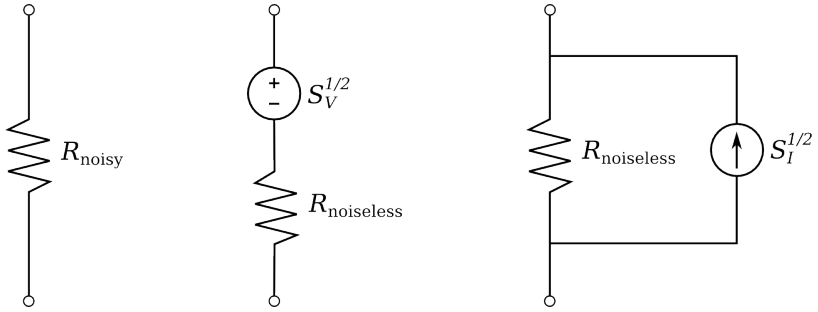

Figure 3.1: Equivalent circuits for the thermal noise in a resistor. A noisy resistor (a) can be represented as a noiseless resistor and a noise voltage source in series (b), or as a noiseless resistor in parallel with a noise current source (c).

fully resistive. However, if the circuit has reactive components, the spectrum is not white. For example, in Ref. [49], the frequency-dependent spectral density for Johnson–Nyquist voltage in an RL system is

$$S_V(f) = \frac{4\,k_{\mathrm{B}}TR}{1+(2\pi Lf/R)^2}\ , \tag{3.5}$$

and for the current

$$S_I(f) = \frac{4\,k_{\mathrm{B}}T}{R}\frac{1}{1+(2\pi Lf/R)^2}\ . \tag{3.6}$$

We see that, at low frequencies, the frequency-dependent spectra behave approximately as white noise. When the frequency has increased to $f = R/(2\pi L)$, the spectral densities have decreased to half their zero-frequency value. This frequency is called the cut-off frequency.

3.3 Thermal magnetic noise from conducting materials

Thermal agitation of the charge carriers in electrical conductors give rise to the fluctuating electromagnetic fields according to Ampère's law $\nabla \times \vec{B} = \mu_0 \vec{J}$. This magnetic noise may limit sensitive field measurements. For example, in SQUID-based measurements, thermal magnetic noise arising from the metallic structures of the cryostat, the magnetically shielded room or

MRI coils may interfere with the desired signal if an excessive amount of conducting material is close to the sensors.

Thermal magnetic noise has been studied over the years both analytically and numerically. The following subsections provide a review about a few of the methods for modeling the thermal magnetic noise and the effect of the conductor shape presented in the literature.

3.3.1 Noise modeling methods in literature

The thermal noise current in a small separate resistor is simple to calculate using Eq. (3.3). However, in case of larger surface or volume conductors, the patterns of thermal noise currents become complicated, not to mention the analysis of the magnetic fields generated by those currents. Therefore, different approaches have been presented in order to analyze thermal magnetic noise.

Until the beginning of the 1980s, the research on thermal magnetic noise was limited only to experimental studies or highly simplified models. Vant-Hull *et al.* [50] as well as Harding and Zimmerman [51] studied electromagnetic normal modes of a conducting infinite rod and a solenoid. Zimmerman [52] estimated the thermal magnetic noise level inside an aluminum enclosure.

In 1983, Varpula and Poutanen published a theoretical model to estimate magnetic Johnson–Nyquist noise arising from a conductor [45]. They divided the volume conductor into infinitesimal rectangular volume elements in which they placed point current dipoles to represent thermal noise sources. The spectral intensities for each cartesian component of the dipoles were set using Eq. (3.1). The magnetic field caused by these noise dipoles was calculated by considering a frequency as well as a source and field point dependent transfer function for each dipole. Taking into account the fields from all uncorrelated dipoles, they ended up with a formula for the thermal magnetic noise field. The results of experimental tests presented agreed well with the deduced formulas. The drawback of this approach is that the magnetic noise formulas are cumbersome with non-zero frequencies and complicated geometries.

The model presented by Varpula and Poutanen has been revisited and extended in several subsequent studies. Nenonen *et al.* [44] used the model for estimating the thermal noise of helium dewars and magnetically shielded rooms. They also presented formulas for calculating the coupling of noise into different types of pick-up loops as well as calculation of spatial correlation of noise between observation points to ease the analysis. At very low temperatures or high frequencies, *i.e.*, when $hf \gg k_\mathrm{B}T$, the quantum effects begin to dominate, which changes the analysis of thermal magnetic noise. This aspect has been studied using quantum theory by Sidles *et al.*

[53], allowing the study of thermal magnetic noise also, for example, in superconducting materials. The results are relevant, for instance, in magnetic resonance microscopy and quantum computing.

Another approach for modeling thermal magnetic noise was taken by Roth who described Johnson–Nyquist noise on a thin infinite plate by superposition of electrical circuits [54]. The noise currents in the circuits were expressed using stream functions as in fluid-dynamic calculations, and the Fourier expansion of the stream function enabled the division of the total thermal noise current into independent loops whose noise spectral density was determined as in Ref. [49]. Then, Roth derived a formula for the magnetic field of each individual loop and finally calculated the normal component of the total magnetic field and its spectral density. This model yielded similar formulas to those obtained by Varpula and Poutanen in Ref. [45] for simple cases.

An alternative attempt to study thermal magnetic noise is to express the conducting material as a triangular mesh consisting of resistors and noise voltage sources as presented by Sandin *et al.* [55]. The currents in the mesh were analyzed using Kirchhoff's equations, and the magnetic field coupled to a pick-up coil was calculated using the reciprocity principle. Since inductive effects were omitted, the model is restricted to very low frequencies.

3.3.2 Conductor shape

Johnson observed that the conductor shape does not affect the power dissipation due to thermal agitation of charge carriers [46, 47]. Instead, the magnetic-field fluctuations caused by the Johnson–Nyquist currents do depend on the shape of the conductor.

Analytical solutions have been obtained only for simple geometries and approximations, and thus numerical methods are needed when the conductor is even slightly more complicated. Table 3.1 presents the formulas for the z component of the amplitude spectral density of thermal magnetic noise at zero frequency arising from non-magnetic conductors of different shapes. The first formula is for an infinite plate. The formula is for the z component of the RMS noise, but Varpula and Poutanen showed that the other components are

$$S_{B_x}^{1/2} = S_{B_y}^{1/2} = \frac{1}{\sqrt{2}} S_{B_z}^{1/2} \ . \tag{3.7}$$

The other shapes are a finite disk, an infinite array of small electrically insulated disks, a spherical shell, a small solid sphere, and a circular cross-section wire. The variables in the formulas correspond to the ones in the figures, and the observation points are marked as crosses. For the infinite

Conductor geometry	$S_{B_z}^{1/2}$	Ref.
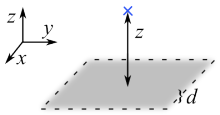 infinite plate	$\mu_0\sqrt{\frac{\sigma k_\mathrm{B}T}{8\pi}\frac{d}{z(z+d)}},\ z>0$	[45, 54, 56]
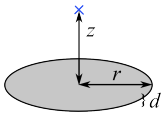 finite disk	$\mu_0\sqrt{\frac{\sigma k_\mathrm{B}Td}{8\pi z^2}}\frac{1}{1+z^2/r^2},\ z\gg d$	[56]
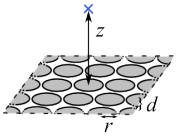 infinite array of disks	$\mu_0\sqrt{\frac{3\sigma k_\mathrm{B}Td}{2048\pi}}\frac{2r}{z^2},\ z\gg 2r$	[56]
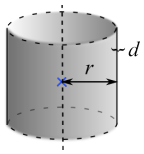 infinite cylinder	$\mu_0\sqrt{\frac{3\sigma k_\mathrm{B}T}{16}\frac{d}{r^2}},\ r\gg d$	[56]
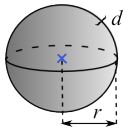 spherical shell	$\mu_0\sqrt{\frac{2\sigma k_\mathrm{B}T}{3\pi}\frac{d}{r^2}},\ r\gg d$	[56]
 small solid sphere	$\mu_0\sqrt{\frac{4\sigma k_\mathrm{B}T}{15\pi}}\frac{r^{\frac{5}{2}}}{z^3},\ z\gg r$	[56]
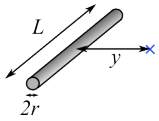 circular cross-section wire	$\mu_0\sqrt{\frac{3\sigma k_\mathrm{B}T}{128}}\frac{r^2}{y^{5/2}}, r\ll y\ll L$	[56]

Table 3.1: Proposed exact and approximate formulas of thermal magnetic noise with different shapes for conducting non-magnetic material. In all the figures, the z axis points upwards and the z component of the field is measured at the points marked as crosses.

array of small disks, the small solid sphere, and the circular cross-section wire, it is assumed that the distance between the observation point and the conductor is much larger than the size of the conductor. In addition, more complicated but analytical formulas for two infinite conducting slabs and a closed finite cylinder can be found in Refs. [44] and [56], respectively.

3.4 Reduction of dewar noise

As explained in Sec. 2.5, the dewar noise is thermal magnetic noise arising from the multi-layer insulation and radiation shields of the cryostat. The level as well as reduction of the dewar noise has been reported in several studies.

Reducing the amount of conductors, *i.e.*, the number of thermal shields and superinsulation layers is an obvious way to reduce the noise level. Especially the insulation in the bottom part of the dewar closest to the sensors is crucial. However, the trade-off is that the helium boils off faster. Since a short holding time is impractical and expensive and may limit the measurement time, the amount of metallic parts cannot be reduced to zero.

The thermal magnetic noise level can be reduced by avoiding large structures in metallic shields. This way, one avoids the largest noise current loops, and the magnetic noise level drops faster with distance. Thus, it is beneficial to break metallic materials into small fragments that are insulated from each other [44, 57].

In refrigerated shields, a continuous copper shield can be cut into narrow strips or thin wires. Nenonen *et al.* [44] placed a sheet of 0.3 mm copper wires next to each other outside the dewar bottom and no change in the noise spectrum was observed in their dc SQUID gradiometer system in 1996. A multifilament wire or an insulated copper wire mesh [58] can be used as a radiation shield with a lower level of noise. Also, one can choose the material of the cooled shield to have low electrical conductivity to decrease the amplitude of Johnson–Nyquist currents. For example, alumina (aluminum oxide, Al_2O_3) has been reported to be suitable for this purpose [59].

The noise from the MLI layers can be reduced by crinkling the sheet [60]. This way, the isolated areas are estimated to be $5\,\mathrm{mm} \times 5\,\mathrm{mm}$. In addition, vapor depositing aluminum on a woven textile reduces the electrically conductive paths efficiently. In Ref. [59], the continuous areas were estimated to be $10\,\mu\mathrm{m} \times 300\,\mu\mathrm{m}$. The conductive layer of the MLI sheets can also be cut into into small squares that are electrically isolated from one another. Mayrhofer *et al.* [61] measured the white noise contribution of 20 layers of aluminum sheet at room temperature with 1-cm^2 patches using a first-

order axial gradiometer and detected a noise amplitude of approximately $1\ \mathrm{fT}/\sqrt{\mathrm{Hz}}$.

One successful example of an extremely low-noise dewar was reported by Seton *et al.* [59] in 2005. They designed and built a low-noise cryostat for SQUID-based MRI system. The radiation shield was constructed from an alumina disk and alumina rods, whereas the superinsulation was of the already-mentioned aluminized woven polyester sheets. This solution reduced the noise down to a few tens of attotesla ($10^{-18}\ \mathrm{T}$). Their dewar design has been replicated in several subsequent low-noise cryostat constructions [62–64].

Chapter 4

Methods

As discussed in Sec. 3.4, the desired dewar noise level can be achieved by a small number of insulating layers and breaking the continuous metallic sheets into small electrically insulated patches. However, these actions reduce the performance of the thermal insulation and causes increase in helium boil-off. Thus, there is a trade-off between a low noise level and a low boil-off rate, which is not trivial to optimize.

As mentioned in Sec. 3.4, aluminized woven fabric can be used for constructing a low-noise dewar. However, although the material is experimentally tested to be appropriate, there is still a lack of detailed studies and theoretical understanding of, *e.g.*, how small the isolated areas should be, and how many layers one can place in the vacuum space of the dewar without exceeding the noise limits. Another option is to use patched aluminum sheets, which is also considered as commercially attractive.

In our simulations, the multi-layer insulation is modeled as patched aluminum sheets, *i.e.*, thin aluminum layers are cut into rectangular areas with a tiny gap between the patches acting as an electrical insulation. For such a configuration, the methods to estimate the boil-off and thermal noise will be described in this chapter in order to ease the design of the new ultra-low-noise measurement dewar.

4.1 Helium boil-off model

Heat transferred from the warm parts of the dewar to the helium reservoir causes boiling of the liquid helium. The evaporated helium gas flows out of the system via a helium-evaporation line. The helium is lost if not collected in a helium-recycling system.

Let us assume that conductive and convective heat leaks are negligible.

Thus, the heat leak calculations are restricted to consider only radiative heat transfer. In addition, as explained in Sec. 2.4, the heat leak can be reduced by inserting multi-layer insulation and cooled radiation shields in the vacuum space. Their effect on reducing the heat leak will be studied in more detail in the following.

Let us first consider the heat transfer between two large parallel surfaces close to each other (see Fig. 4.1a). The surfaces are at temperatures T_{H} and T_{L}, having emissivities ε_{H} and ε_{L}. The radiative heat flux between the bodies can be calculated using Eq. (2.8). When the emissivity factor and the view factor for two large parallel plates are taken into account, the heat transfer rate from the warmer surface to the cooler one is given by (see for example Ref. [31] or Ref. [29])

$$\dot{Q} = A\sigma_{\mathrm{SB}} \left(T_{\mathrm{H}}^4 - T_{\mathrm{L}}^4\right) \left(\frac{1}{\varepsilon_{\mathrm{H}}} + \frac{1}{\varepsilon_{\mathrm{L}}} - 1\right)^{-1} , \tag{4.1}$$

where σ_{SB} is the Stefan–Boltzmann constant and A is the area of one surface.

If we add N floating reflecting layers between the surfaces (see Fig. 4.1b), the radiative heat transfer is reduced. The emissivities of the insulation layers depend on temperature, and different sides of the layers may have different emissivities. The shield emissivities are denoted as $\varepsilon_{n,1}$ and $\varepsilon_{n,2}$, where $n = 1, \ldots, N$ is the index of the layer starting from the layer closest to the cold surface. For each pair of adjacent layers, one can write the heat transfer between them as in Eq. (4.1), which leads to a system of $N + 1$ equations. In the steady state, the same amount of heat passes through each layer, so $\dot{Q}$ is same for each equation. Adding all $N + 1$ equations together and rearranging the components leads to:

$$\dot{Q}_{\mathrm{N}} = \frac{A\sigma_{\mathrm{SB}} \left(T_{\mathrm{H}}^4 - T_{\mathrm{L}}^4\right)}{\dfrac{1}{\varepsilon_{\mathrm{H}}} + \dfrac{1}{\varepsilon_{\mathrm{L}}} - 1 + \displaystyle\sum_{n=1}^{N} \left(\frac{1}{\varepsilon_{n,1}} + \frac{1}{\varepsilon_{n,2}} - 1\right)} . \tag{4.2}$$

Thus, the reduction in the heat transfer by the MLI is evident from the summation term in the denominator. The lower the emissivity values of the shields, the more the heat leak is reduced.

Layer temperatures can be determined using the same steady-state approximation as above. Setting $\dot{Q}_{\mathrm{N}}$ equal to the heat transfer rate between the cool surface and the first superinsulation layer, one can solve the temperature of the first shield T_1. Continuing similarly for the next shields and using recursively the temperature of the previous shield, we end up with a

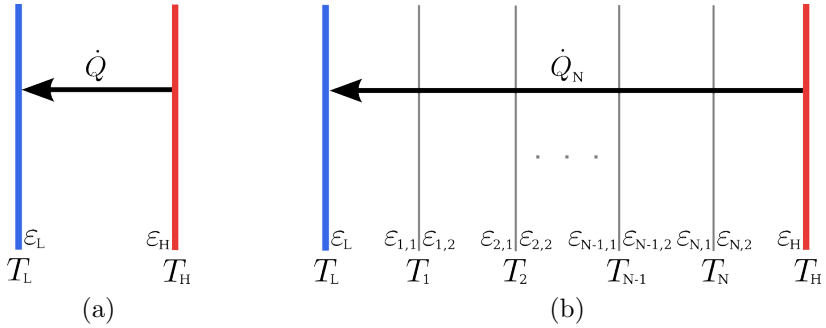

Figure 4.1: A schematic drawing showing the structures and variables used in calculation of the radiative heat transfer between two surfaces. (a) The case without any MLI layers. (b) Case with N insulation layers between the surfaces.

general formula for the shield temperatures:

$$T_n = \left[\frac{\dot{Q}}{A\sigma_{\mathrm{SB}}} \left(\frac{1}{\varepsilon_{\mathrm{L}}} + \sum_{i=1}^{n} \frac{1}{\varepsilon_{i,1}} + \sum_{i=1}^{n-1} \frac{1}{\varepsilon_{i,2}} - n \right) + T_{\mathrm{L}}^4 \right]^{\frac{1}{4}} \tag{4.3}$$

In case all the emissivities are the same ($\varepsilon_{\mathrm{H}} = \varepsilon_{\mathrm{L}} = \varepsilon_{n,1} = \varepsilon_{n,2} = \varepsilon$), the equations become simpler. The heat leak with N layers of insulating sheets results in

$$\dot{Q}_{\mathrm{N}} = \frac{A\sigma_{\mathrm{SB}} \left(T_{\mathrm{H}}^4 - T_{\mathrm{L}}^4 \right)}{(N+1) \left(\frac{2}{\varepsilon} - 1 \right)} \, . \tag{4.4}$$

which indicates that the heat leak is reduced by a factor of $N+1$ compared to the situation with no added insulation layers. In this case, the temperatures of the layers are given by

$$T_n = \left[\frac{n T_{\mathrm{H}}^4 + (N - n + 1) \, T_{\mathrm{L}}^4}{N+1} \right]^{\frac{1}{4}} \, . \tag{4.5}$$

In the heat-leak and temperature calculations, the values for the surface emissivities are needed. Since we intend to use patched aluminum sheet, we lose an amount of aluminum area when making the cuts between the patches and the underlying polyester becomes visible. Therefore, the emissivity of a patched sheet is somewhere between the emissivities of a continuous aluminum sheet $\varepsilon_{\mathrm{Al}}$ and a polyester film $\varepsilon_{\mathrm{PES}}$. Let us assume that the emissivity increases linearly as a function of the lost aluminum area. Thus, the emissivity of the patched aluminum sheet can be expressed as

$$\varepsilon_n = (\varepsilon_{\mathrm{Al}} - \varepsilon_{\mathrm{PES}}) \, A_{\mathrm{prop}} + \varepsilon_{\mathrm{PES}} \, , \tag{4.6}$$

where A_{prop} is the ratio of the remaining area of the aluminum on the sheet and the total area of the sheet. When $A_{\text{prop}} = 1$, the emissivity is equal to that of aluminum, and when $A_{\text{prop}} = 0$, the emissivity corresponds to the one of polyester.

As mentioned in Sec. 2.4, the emissivity of a surface is a complex concept and usually not accurately known. Thus, one needs to employ the experimentally obtained values from the literature. According to Ref. [65], the total hemispherical emissivity values of aluminum changes approximately between 0.002 and 0.02 below room temperature. For simplicity, and in order not to underestimate the boil-off, the room-temperature value 0.02 is used. Emissivity of both fiberglass and polyester is approximately 0.75.

After calculating the radiative heat transfer rate through MLI layers, we can calculate the amount of boiling helium. The amount of heat needed for evaporating liquid helium of mass m can be calculated using the specific latent heat of vaporization L_{v} as follows:

$$Q = mL_{\text{v}} \, . \tag{4.7}$$

Substituting Eq. (4.2) into Eq. (4.7), and using the definition of density, $\rho = m/V$, yields the boil-off rate of a multilayer insulation system

$$\dot{V} = \frac{\dot{Q}_{\text{N}}}{\rho L_{\text{v}}} \, . \tag{4.8}$$

If we add one or several cooled radiation shields between the floating superinsulation layers, the heat leak can be greatly reduced, as mentioned in Sec. 2.4. Let us consider the effect of one cooled radiation shield at temperature T_{S}. A schematic diagram of the heat flows in this kind of system is shown in Fig. 4.2. The radiative heat fluxes Q_1 from the outer vessel to the cooled shield and Q_2 from the cooled shield to the inner vessel with MLI shields between the surfaces can be calculated using Eq. (4.2). With a cooled shield, the heat leak causing the helium boil-off is given only by Q_2.

Due to the cooled shield, the heat flux $Q_1 - Q_2$ is intercepted and conducted to the heat exchanger. Cooling can be enhanced by choosing a shield material with a good axial thermal conductivity so that the heat is effectively transferred to the heat exchanger. From the heat exchanger, the heat is removed by using the enthalpy of the vaporized helium gas.

4.2 Eddy-current thermal noise model

This section describes methods to estimate the thermal magnetic noise arising from the Johnson–Nyquist currents flowing on thin conducting structures.

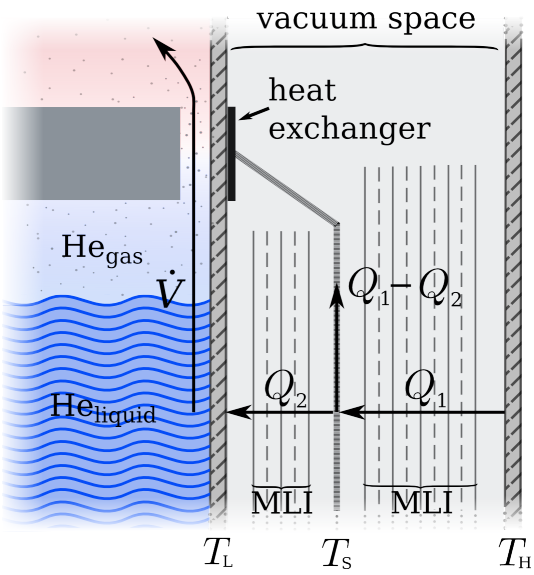

Figure 4.2: A schematic drawing of heat fluxes in a dewar with a vapor-cooled radiation shield between MLI.

The method is based on the eddy-current model presented by Zevenhoven [66] and Zevenhoven *et al.* [67]. In the context of these publications, the model is used for the analysis of the eddy current transient problems in ULF MRI.

On a thin conducting object, current patterns can be expressed using a surface current-density $\vec{K}$. It can be expressed using a scalar function Ψ as follows

$$\vec{K} = \nabla\Psi \times \vec{n}\,, \tag{4.9}$$

where $\vec{n}$ is a normal vector of the surface. Any possible Ψ on the thin structure can be formed using a linear combination of suitable basis functions $\sum_k j_k\psi_k$, leading to

$$\vec{K}(\vec{r}\,') = \sum_k j_k \nabla\psi(\vec{r}\,') \times \vec{n}(\vec{r}\,')\,, \tag{4.10}$$

where $\vec{r}\,'$ is a position vector on the surface and j_k a coefficient of the basis function in question. The eddy-current patterns can be considered as electrical circuits and the coefficient j_k as a current amplitude in circuit k.

On a square patch with a size of $a \times a$ placed on the xy plane, a function basis fulfilling the boundary conditions is a 2D Fourier basis expressed as

$$\psi_{n,m}(x,y) = \frac{2\sin\left(\frac{n\pi x}{a}\right)\sin\left(\frac{m\pi y}{a}\right)}{\pi\sqrt{n^2+m^2}}\,, \tag{4.11}$$

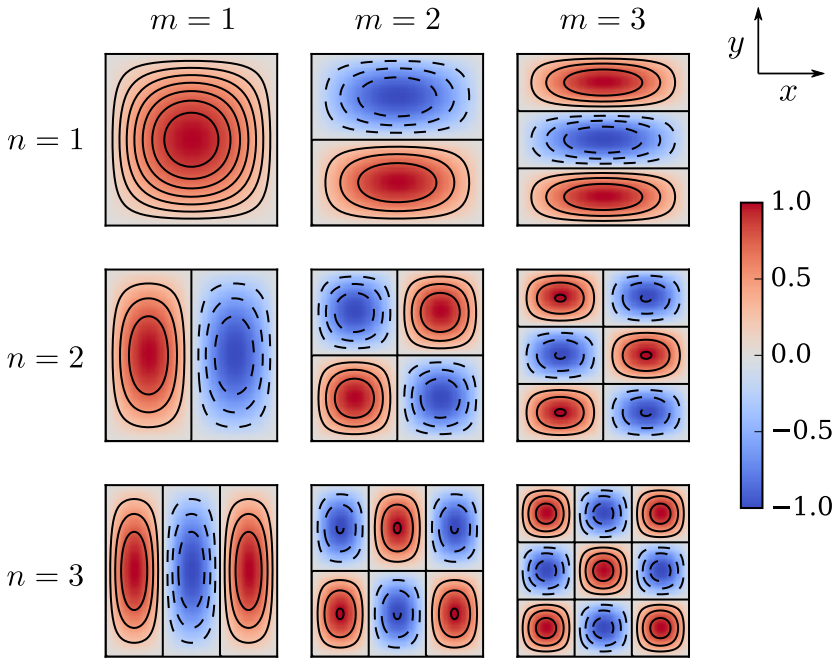

Figure 4.3: Examples of the normalized basis function patterns and current patterns. Current flows on the isocontours of the basis function patterns. On the solid lines, current flows clockwise and on the dashed lines counterclockwise.

where n and m are positive integer orders of the basis functions. Examples of these basis functions are visualized in Fig. 4.3. The surface current pattern can be approximated using a finite number of basis functions in the linear combination.

When calculating the thermal magnetic noise, j_k can be substituted by the noise current amplitude spectral density $S_{I,k}^{1/2}$ given by Eq. (3.4), and then the magnetic field can be calculated using the Biot–Savart law

$$\vec{B}_k(\vec{r}) = \frac{\mu_0}{4\pi} \int_S \frac{\vec{K}_k(\vec{r}') \times (\vec{r} - \vec{r}')}{|\vec{r} - \vec{r}'|^3} dS' \,, \tag{4.12}$$

where μ_0 is the vacuum permeability, $\vec{r}$ the field point, and S the surface of the patch. This gives the field amplitude spectral density contributed by the circuit k:

$$S_B^{1/2}(\vec{r}) = \beta_k(\vec{r}) S_{I,k}^{1/2} \,, \tag{4.13}$$

where $\beta_k(\vec{r})$ is the magnetic field at a field point $\vec{r}$ generated by a unit current in circuit k.

To estimate the thermal magnetic noise generated by one patch, we use a finite number of basis functions up to an order of $n = m = M$. Since the basis functions are orthogonal, their combined contribution to the field noise can be calculated as follows

$$S_B^{1/2}(\vec{r}) = \sqrt{\sum_k \left[\beta_k(\vec{r}) S_{I,k}^{1/2}\right]^2}. \tag{4.14}$$

For a multi-patch system, the noise current patterns on all the patches can be assumed to be uncorrelated, and the total noise level can be calculated using Eq. (4.14), summing over all the current patterns in all patches.

For calculating the value of $S_{I,k}^{1/2}$ on each patch on each layer of the MLI, the temperature distribution is given by Eq. (4.3). In addition, one needs the resistance values for each current pattern. They can be expressed as a sheet resistance $R_k = (\sigma d)^{-1}$, where σ is the electrical conductivity and d the thickness of the surface. The electrical conductivity of pure aluminum as a function temperature is shown in Fig. 4.4. The data were taken from Ref. [68] and interpolated using third-order spline functions. The electrical conductivities corresponding to the calculated layer temperatures can be interpolated similarly. As can be seen from the figure, the conductivity increases dramatically at low temperatures. However, according to the same reference, the conductivity values vary greatly below 50 K depending on the purity of aluminum.

The described noise calculation method holds for zero- or very low-frequency noise currents and gives the white noise level of the thermal magnetic noise. However, the model is applicable also to the calculation of the dynamics of the currents and fields on higher frequencies. Then, the self- and mutual inductance of the circuits need to be calculated. To further simulate the dynamics of the system, one needs to solve a differential equation system. To use Eq. (4.14) for the total noise from the uncorrelated sources, in the dynamic case, one can decouple the system using the eigenvalue decomposition. In addition, the decomposition allows a more efficient calculation of the dynamics. However, this leads to an issue with systems having several layers at different temperatures, since the system becomes non-Hermitian. In addition, with a large number of patches and basis functions, the simulations become computationally heavy.

Even though the model is suitable for the alternating current analysis, the frequencies cannot be too large. The theory is valid for low frequencies, and limited at least by the following two factors. First, the model assumes

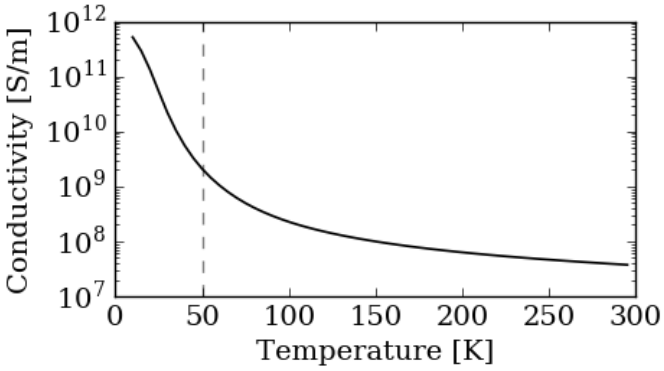

Figure 4.4: Electrical conductivity of pure aluminum as a function of temperature.

that the Maxwell's displacement current is negligible. This is a valid approximation at low frequencies, but at high frequencies, it cannot be omitted. Second, if the skin depth of the conducting layer becomes smaller than the thickness, the approximation of the thin layer breaks down.

Chapter 5

Results

This chapter shows the results of the dewar noise and boil-off simulations based on the models presented in Ch. 4. First in Sec. 5.1, the simulations for validating the noise model are presented. Sec. 5.2 describes the simulation results, which reveal the effect of the number of insulating layers and the patch size to the noise amplitude and helium boil-off. In addition, noise coupling to a superconducting pick-up loop is simulated.

The simulations were carried out with numerical tools in Python 3 based on the NumPy and SciPy packages.

5.1 Noise model validation

To validate the noise modeling method presented in Sec. 4.2, the simulations were compared with the analytical formula of the noise emanating from a thin infinite plate (Table 3.1). Both the analytical and simulated noise are calculated with a frequency $f = 0$, which gives an upper limit for thermal noise. With a plate temperature $T = 300\,\mathrm{K}$, the corresponding aluminum conductivity $\sigma = 3.66 \times 10^7\,\mathrm{S/m}$, a plate thickness $d = 100\,\mu\mathrm{m}$, and an observation point $z = 1\,\mathrm{cm}$ above the origin, the analytical formula gives $97.1\,\mathrm{fT}/\sqrt{\mathrm{Hz}}$ for the z component of the amplitude spectral density of the thermal magnetic noise.

In the simulation, a $15\,\mathrm{cm} \times 15\,\mathrm{cm}$ plate was used to mimic an infinite plate and its noise amplitude was calculated using the same parameters as in the analytical case. The maximum order of the basis functions used in the simulations was varied, and the results are presented in Fig. 5.1. The dots in the figure represent the simulated noise amplitudes as a function of a so-called detail scale parameter D of the eddy-current model divided by z. Here, the detail scale parameter is a concept that describes the smallest detail in

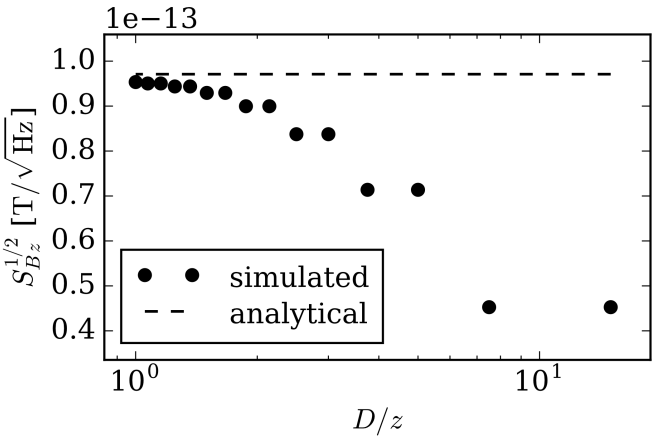

Figure 5.1: Thermal magnetic field noise amplitude as a function of D/z. The dashed line is the analytical value for the thermal magnetic noise arising from an infinite plate, and the dots represent the approximate amplitude spectral densities from a large plate calculated using the simulation model presented in Sec. 4.2. The thickness of the plate is 100 µm and $z = 1$ cm.

the basis function pattern, corresponding to approximately $D = a/M$, where M is the maximum order of the basis functions and a is the side length of a square patch. For example, if the detail scale is $D = 1$ cm, and the patch size 3 cm, the maximum order is $M = (3\,\text{cm})/(1\,\text{cm}) = 3$.

As can be seen from Fig 5.1, reducing the detail scale parameter, *i.e.*, increasing the maximum order, the noise amplitude approaches the theoretical prediction. When the maximum order is 15 and the corresponding detail scale parameter 1 cm, the simulated noise amplitude is $95.3\,\text{fT}/\sqrt{\text{Hz}}$. The relative error between the analytical and simulated noise amplitudes is then 1.8%.

The figure also reveals that the even-order basis functions do not contribute to the z component of the noise when the measurement point is above the origin. However, for the x and y components, they do have an influence. With the smallest calculated detail scale parameter, the simulated x and y components are both 65.0 $\text{fT}/\sqrt{\text{Hz}}$. The relative error to the analytical value of the x and z components calculated using Eq. (3.7) is 5.3%, which is presumably due to the finite size of the simulated plate. According to the results presented above, the simulation model is suitable for estimating the thermal magnetic noise arising from Johnson–Nyquist currents within thin conductors.

An interesting unknown is the order of the basis functions needed with given values for a and z when modeling a finite-sized plate. As can be seen from Fig. 5.1, with a 15 cm $\times$ 15 cm plate, even the first basis function $n = m = 1$ (corresponding to the dot with the largest detail scale parameter in the figure) explains approximately half of the noise. After a certain order, the addition of higher-order functions does not significantly affect the noise amplitude.

To estimate the required number of basis functions, the noise was calculated using different patch sizes and different numbers of the basis functions, varying the distance from the surface. The material properties were kept the same as in the previous calculation. For a few patch sizes, the relative differences between the obtained noise amplitudes and the noise calculated using the smallest D in each case were computed. The results as a function of D/z are depicted in Fig. 5.2a. We see that, when $D/z \leq 2$, the relative differences are below 4.2%. Alternatively, if we set $D/z \leq 1$ and $M \geq 3$, the errors are below 0.6%. The further from the plate the observation point, the fewer basis functions on a patch are needed.

Another interesting thing is the required plate size for calculating the noise in one point. If calculating the noise above the center point of a large plate, a smaller plate can be used as an approximation. The accuracy of this approximation was studied by changing L, the size of the patched plate, and calculating the difference of the noise amplitude compared to the noise from the largest plate in each case. Several cases with different combinations of a and z were calculated, still keeping the same material properties. Representative examples of the relative differences are depicted as a function of L/z in Fig. 5.2b. As can be seen, the larger the ratio L/z, the smaller is the difference. When $L/z \geq 2$, relative differences are below 0.6%. This also verifies an intuitive fact: the closer the observation point is to the surface, the smaller a plate is needed for an approximation of a large or infinite plate.

5.2 Effect of patch size and number of layers

We already know that a smaller patch size and number of MLI layers lead to lower noise level, and that the trade-off is in the increased boil-off rate. Let us next study the effect of the patch size a, and the number of layers N on the level of thermal magnetic noise and boil-off in more detail.

To use realistic properties of MLI layers, the thickness of aluminum is set to 100 nm for the following simulations. The rules for the number of the basis functions and the plate size formed in the previous section were fulfilled for ensuring sufficiently accurate noise calculations.

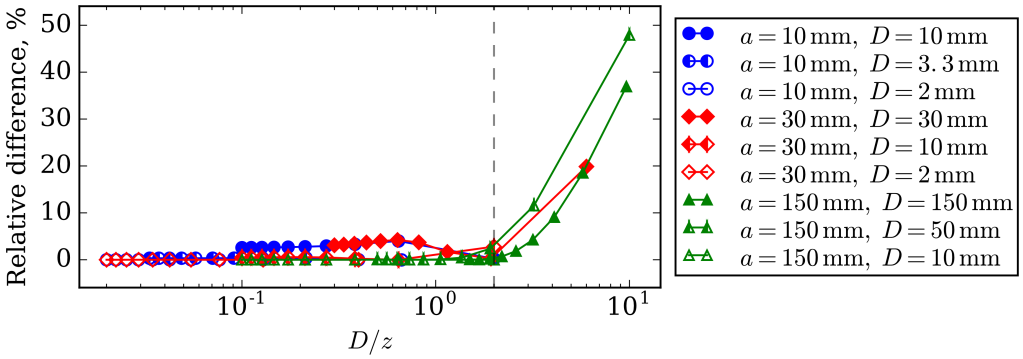

(a)

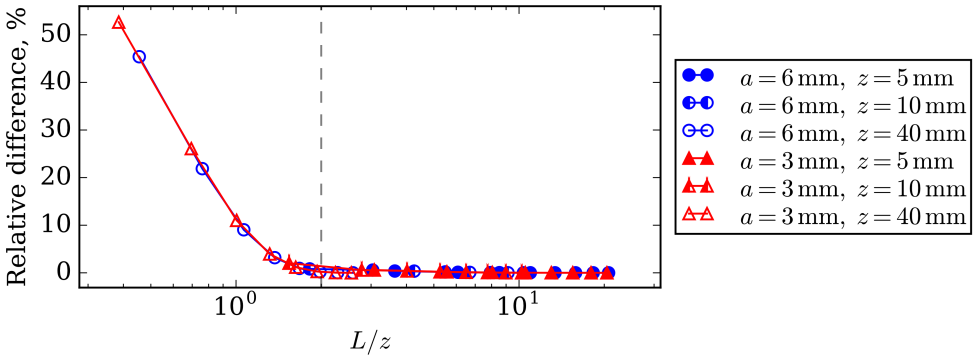

(b)

Figure 5.2: (a) The effect of D/z for the calculation of the noise amplitude spectral density. The results are presented as relative differences between the noise amplitudes and the corresponding value calculated using the largest number of basis functions (empty markers). (b) The influence of the plate size to the noise calculation. The relative differences between the noise amplitude and the corresponding value with the largest plate size in a few example cases with fixed a and z as a function of L/z.

5.2.1 Noise

The effect of the patch size on the noise level was studied simply by simulating a single layer patched sheet and varying the patch size. Fig. 5.3 shows the results calculated with $T = 100\,\mathrm{K}$, $z = 1\,\mathrm{cm}$, and a ranging between 0.5 mm and 10 mm. As presumed, the noise amplitude spectral density decreases with a decreasing patch size. Interestingly, the noise becomes lower than $0.1\,\mathrm{fT}/\sqrt{\mathrm{Hz}}$ only with a patch size of $a \approx 1\,\mathrm{mm}$ or smaller.

For comparison, the noise arising from an infinite array of small disks calculated by an analytical approximate formula (see Table 3.1) is visualized with a dashed line. The horizontal axis corresponds to the diameter $2r$ of the small disk. The approximation is believed to hold when $z \gg 2r$. This is revealed also in Fig. 5.3, since the larger the diameter of the disk, the more it differs from the accurate simulation. This results validates the approximate formula presented in Ref. [56].

Next, the increase of noise with the number of layers N in the MLI stack was studied. Fig. 5.4 shows the noise calculated with $N = 1$ up to $N = 15$ and $a = 1\,\mathrm{mm}$, 5 mm, and 1 cm. Temperature distributions in each case with each N were calculated using Eq. (4.3). The layer spacing was 0.5 mm and $z = 1\,\mathrm{cm}$. With $N = 15$, the amplitude spectral density of the noise was $0.17\,\mathrm{fT}/\sqrt{\mathrm{Hz}}$, $1.0\,\mathrm{fT}/\sqrt{\mathrm{Hz}}$, $2.2\,\mathrm{fT}/\sqrt{\mathrm{Hz}}$ the for $a = 1\,\mathrm{mm}$, 5 mm, and 1 cm, respectively.

5.2.2 Boil-off

As discussed previously, decreasing the number of reflective layers increases the helium boil-off. In addition, the smaller the patch size, the more aluminum surface is lost with a fixed patch spacing, resulting in an increase in emissivity, and thus in the boil-off. The same cases as in the noise simulation in the previous section were used to approximate the boil-off rate.

The effect of the patch size on the helium boil-off rate is visualized in Fig. 5.5a. In the simulation, an insulation layer was placed in the vacuum space. Its temperature was calculated using Eq. (4.3), and the helium boil-off rate using Eqs. (4.2) and (4.8). As seen in the figure, the boil-off is higher with the small patch sizes. The emissivities calculated using Eq. (4.6) as a function of the patch size are depicted in Fig. 5.5b.

Fig. 5.6 presents the effect of the number of insulating layers on the boil-off. As can be seen, with $N = 15$, the BOR is reduced by a factor of approximately 10 compared to the case with only one layer. With 15 layers of $1\,\mathrm{mm}^2$ patched sheets, the boil-off rate is $125\,\mathrm{l/day/m}^2$. If a cooled radiation shield with a fixed temperature of 120 K is added between the fifth and the

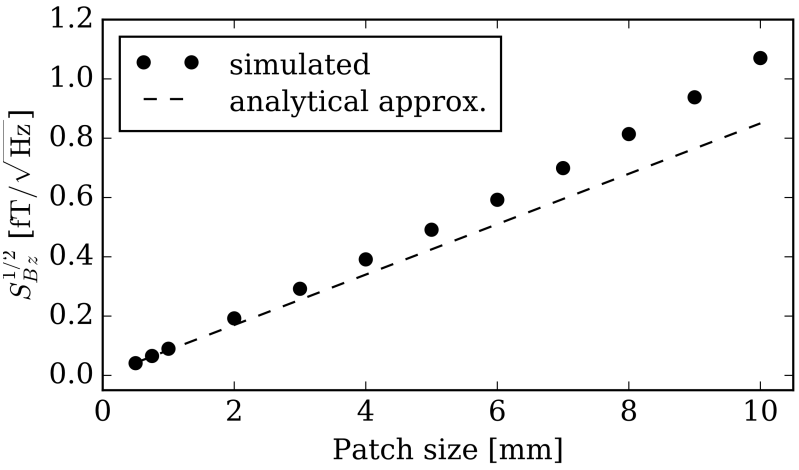

Figure 5.3: Amplitude spectral density of thermal magnetic noise as a function of patch size is presented with black dots. For comparison, an analytical approximate formula of an infinite array of small disks with varying disk diameter is illustrated as dashed line.

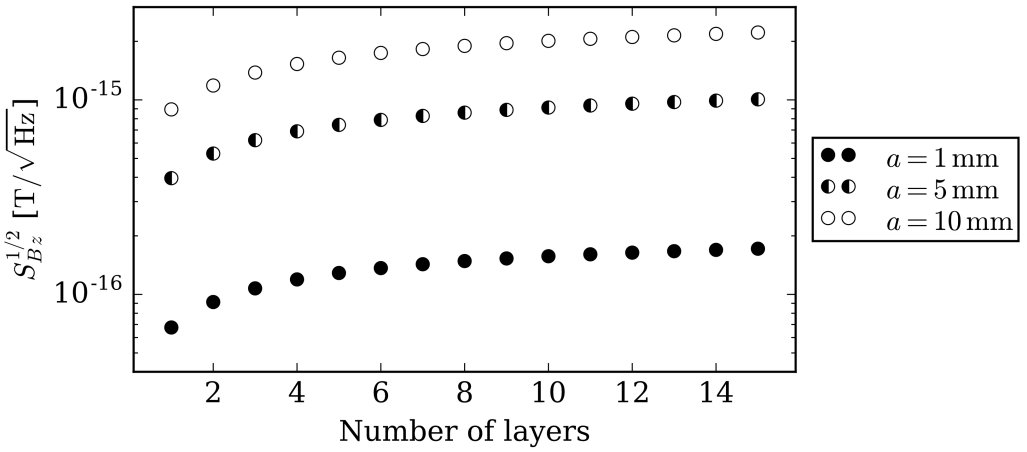

Figure 5.4: Amplitude spectral density of the thermal magnetic noise as a function of the number of the MLI layers. Cases with $a = 1\,\text{mm}$, $a = 5\,\text{mm}$, and $a = 1\,\text{cm}$ are visualized.

sixth layer, the boil-off reduces to $10\,\text{l/day/m}^2$.

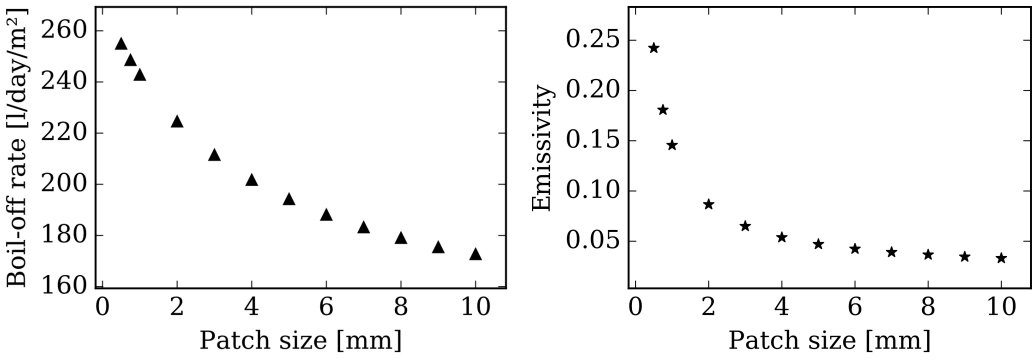

(a) (b)

Figure 5.5: (a) Boil-off rate as a function of the patch size with one insulation layer in the vacuum space. (b) Emissivity as a function of patch size.

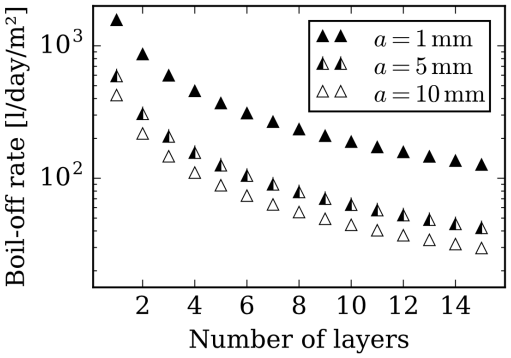

Figure 5.6: Boil-off rate as a function of the number of the MLI layers. Cases with $a = 1\,\mathrm{mm}$, $a = 5\,\mathrm{mm}$, and $a = 1\,\mathrm{cm}$ are visualized.

5.3 Coupling to a pickup loop

The previous results were calculated for a point-like sensor. Fig. 5.7 shows the coupling of the thermal magnetic noise from a patched sheet to a finite-sized superconducting loop. In this example, the loop is a rectangular magnetometer with varying loop side length, placed 1 cm above the patched sheet. The patch size is 5 mm, the plate thickness 100 nm, and the plate temperature 100 K.

In the simulation, the flux noise was calculated separately for each basis function using Eq. (2.4). The contribution from all the current patterns from

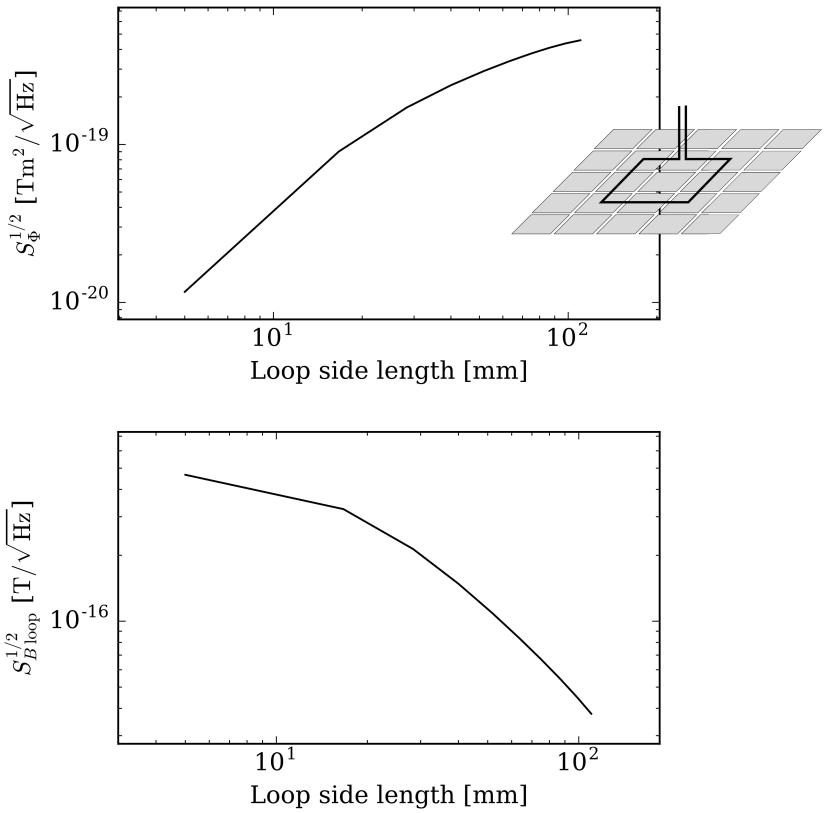

Figure 5.7: Thermal magnetic noise from a patched sheet with $a = 5$mm seen by a rectangular magnetometer 1cm above the sheet. The figure on the top shows the spectral density of the flux noise as a function of the loop side length. The bottom figure shows the corresponding field noise.

all the patches was then summed quadratically. These results are visualized in the upper plot of Fig. 5.7. The bottom figure shows the same data as the field noise seen by the loop, obtained by dividing the flux noise by the effective area of the magnetometer. It can be seen that the field noise decreases with increasing loop size. In this case, the noise level of $0.1\,\text{fT}/\sqrt{\text{Hz}}$ can be reached with a magnetometer loop side length of approximately 5.5 cm.

Chapter 6

Conclusion

In this thesis, the thermal magnetic noise arising from the thermal motion of the charge carriers in electrically conducting structures was studied. In SQUID-based magnetic-field measurements, this noise source can be dominant if not carefully considered. Regarding noise, crucial parts of the system are the superinsulation and the cooled shield, since they are often made of metals and placed near the sensors.

Recent and possible future advances in ULF MRI and SQUID sensor technology raise a need for extremely low-noise dewars. In general, the electrically conducting parts of the thermal insulation can be broken into small isolated areas in order to avoid the largest noise-current loops and to reduce the dewar noise level. However, there are currently no detailed studies about the effect of the size of the isolated area and the number of the insulation layers on the thermal magnetic noise.

To respond to this lack of information, this thesis describes methods for accurate calculation of the noise arising from patched superinsulation. The simulations showed the effects of the patch size and the number of the layers on the noise level. The simulation of the influence of the patch size also provided verification for the approximate formula presented in Ref. [56]. In addition, the simulations of the coupling of thermal magnetic noise into a pick-up loop were performed. Since the structuring of the insulation layers increases the boil-off rate of the liquid helium, the estimation of the boil-off was also included in the simulations.

The noise simulation method was validated by comparing the simulated noise level arising from a relatively large finite plate to a theoretical value for the noise from an infinite plate. The simulations agreed well with the theoretical prediction. The boil-off model gave rough estimates about the boil-off and it could be validated experimentally by comparing the results with the boil-off of a dewar with known parameters.

Based on the simulation results, a single 100-nm thick aluminum layer at 100 K needs a patch side length of less than approximately 1 mm to get the noise level down to $0.1\,\mathrm{fT}/\sqrt{\mathrm{Hz}}$ or below, when the observation point is 1 cm above the plate. On the other hand, if for example 15 sheets with 1-mm^2 patches are placed in the vacuum space on the bottom of the dewar, the noise spectral density is still only $0.17\,\mathrm{fT}/\sqrt{\mathrm{Hz}}$ and the corresponding boil-off rate 125 l/day/m^2. With larger patch sizes, the noise contribution can be reduced by using a large pickup loop. For example, the noise level of $0.1\,\mathrm{fT}/\sqrt{\mathrm{Hz}}$ can be reached by using a magnetometer with side length of 5.5 cm, when the patch size is 5 mm.

The simulations were mostly carried out using 100 nm as the thickness of the aluminum layer. If it was possible to make the aluminum layer thinner, it would further reduce the noise. However, the aluminized layer cannot be too thin, since at a certain point, the emissivity value starts to increase, resulting in an increase in the boil-off. The value for the spacing between the isolated patches used in the simulations was 0.1 mm. If it could be made smaller, it would reduce the boil-off particularly with small patches, since not that much area of the aluminium layer would be lost, and thus the increase in emissivity would also be smaller.

In terms of noise, the most strict requirements are for the innermost MLI layer on the dewar bottom, since it is closest to the sensors. The electrical conductivity of aluminum increases with a decreasing temperature and it depends heavily on the purity of aluminum below 50 K. In addition, the RMS of the Johnson–Nyquist noise currents increase with the electrical conductivity, and decrease with the temperature. In case of pure aluminum, the conductivity increases faster than the temperature decrease would reduce the noise. Therefore, we anticipate not placing the innermost MLI layer directly in contact with the helium vessel close to the sensors, especially if the purity of aluminum is not known. If the surfaces are at least slightly apart from each other, they are not in thermal contact. Therefore, the first MLI layer has a higher temperature, and thus a lower noise level.

One could also make smaller patches on the innermost layers and increase the patch size towards the outer layers. This could be done since the temperatures of the outermost layers are higher and they are physically further from the sensors. The optimization of this possibility is left for the future. Another thing that would be interesting to study in the future, is the frequency dependence of the thermal magnetic noise generated by the patched superinsulation. The model used in these noise simulations can also be extended to the dynamic case. In addition, the noise from the cooled radiation shield was not calculated here. If it is made of an electrically conducting material, its contribution to the thermal magnetic noise needs to be taken

into consideration as well.

Patched aluminum sheets are considered as a commercially attractive MLI solution, and therefore studied also in this thesis. However, aluminized woven textile has been empirically proven to be practical for the construction of a low-noise dewar with a reasonable hold-time. If we cannot obtain a low enough noise level using the patched aluminum sheets, such aluminized fabric should be considered as an alternative.

Bibliography

[1] M. Hämäläinen, R. Hari, R. J. Ilmoniemi, J. Knuutila, and O. V. Lounasmaa, "Magnetoencephalography—theory, instrumentation, and applications to noninvasive studies of the working human brain," *Reviews of Modern Physics*, vol. 65, no. 2, pp. 413–497, 1993.

[2] J. Clarke and A. I. Braginski, eds., *The SQUID Handbook Vol. I Fundamentals and Technology of SQUIDs and SQUID Systems*. Wiley-VCH, Weinheim, Germany, 2004.

[3] J. P. Mäkelä, N. Forss, J. Jääskeläinen, E. Kirveskari, A. Korvenoja, and R. Paetau, "Magnetoencephalography in neurosurgery," *Neurosurgery*, vol. 59, no. 3, pp. 493–510, 2006.

[4] E. M. Haacke, R. W. Brown, M. R. Thompson, and R. Venkatesan, *Magnetic Resonance Imaging: Physical Principles and Sequence Design*. New York, USA: John Wiley & Sons, 1999.

[5] Z.-P. Liang and P. C. Lauterburg, *Principles of Magnetic Resonance Imaging: A Signal Processing Perspective*. New York, USA: IEEE Press, 2000.

[6] J. Clarke, M. Hatridge, and M. Mößle, "SQUID-detected magnetic resonance imaging in microtesla fields," *Annual Review of Biomedical Engineering*, vol. 9, pp. 389–413, 2007.

[7] R. H. Kraus Jr, M. A. Espy, P. E. Magnelind, and P. L. Volegov, *Ultra-Low Field Nuclear Magnetic Resonance*. New York: Oxford University Press, 2014.

[8] V. S. Zotev, A. N. Matlashov, P. L. Volegov, I. M. Savukov, M. A. Espy, J. C. Mosher, J. J. Gomez, and R. H. Kraus Jr, "Microtesla MRI of the human brain combined with MEG," *Journal of Magnetic Resonance*, vol. 194, pp. 115–120, 2008.

[9] P. T. Vesanen, J. O. Nieminen, K. C. J. Zevenhoven, J. Dabek, L. T. Parkkonen, A. V. Zhdanov, J. Luomahaara, J. Hassel, J. Penttilä, J. Simola, A. I. Ahonen, J. P. Mäkelä, and R. J. Ilmoniemi, "Hybrid ultra-low-field MRI and magnetoencephalography system based on a commercial whole-head neuromagnetometer," *Magnetic Resonance in Medicine*, vol. 69, pp. 1795–1804, 2013.

[10] S. K. Lee, M. Mößle, W. Myers, N. Kelso, A. H. Trabesinger, A. Pines, and J. Clarke, "SQUID-detected MRI at 132 μT with T_1-weighted contrast established at 10 μT–300 mT," *Magnetic Resonance in Medicine*, vol. 53, no. 1, pp. 9–14, 2005.

[11] S. Hartwig, J. Voigt, H.-J. Scheer, H.-H. Albrecht, M. Burghoff, and L. Trahms, "Nuclear magnetic relaxation in water revisited," *Journal of Chemical Physics*, vol. 135, p. 054201, 2011.

[12] P. T. Vesanen, K. C. J. Zevenhoven, J. O. Nieminen, J. Dabek, L. T. Parkkonen, and R. J. Ilmoniemi, "Temperature dependence of relaxation times and temperature mapping in ultra-low-field MRI," *Journal of Magnetic Resonance*, vol. 235, pp. 50–57, 2013.

[13] J. O. Nieminen, K. C. J. Zevenhoven, P. T. Vesanen, Y.-C. Hsu, and R. J. Ilmoniemi, "Current-density imaging using ultra-low-field MRI with adiabatic pulses," *Magnetic Resonance Imaging*, vol. 32, pp. 54–59, 2014.

[14] P. T. Vesanen, J. O. Nieminen, K. C. J. Zevenhoven, Y.-C. Hsu, and R. J. Ilmoniemi, "Current-density imaging using ultra-low-field MRI with zero-field encoding," *Magnetic Resonance Imaging*, vol. 32, pp. 766–770, 2014.

[15] M. Mößle, S.-I. Han, W. R. Myers, S.-K. Lee, N. Kelso, M. Hatridge, A. Pines, and J. Clarke, "SQUID-detected microtesla MRI in the presence of metal," *Journal of Magnetic Resonance*, vol. 179, no. 1, pp. 146–151, 2006.

[16] R. H. Kraus Jr, M. A. Espy, P. L. Volegov, A. N. Matlachov, J. C. Mosher, A. V. Urbaitis, and V. S. Zotev, "Toward SQUID-based direct measurement of neural currents by nuclear magnetic resonance," *IEEE Transactions on Applied Superconductivity*, vol. 17, no. 2, pp. 854–857, 2007.

[17] R. H. Kraus Jr, P. Volegov, a. Matlachov, and M. Espy, "Toward direct neural current imaging by resonant mechanisms at ultra-low field," *NeuroImage*, vol. 39, pp. 310–317, 2007.

[18] N. Höfner, H.-H. Albrecht, A. M. Cassará, G. Curio, S. Hartwig, J. Haueisen, I. Hilschenz, R. Körber, S. Martens, H.-J. Scheer, J. Voigt, L. Trahms, and M. Burghoff, "Are brain currents detectable by means of low-field NMR? A phantom study," *Magnetic Resonance Imaging*, vol. 29, no. 10, pp. 1365–1373, 2011.

[19] R. Körber, J. O. Nieminen, N. Höfner, V. Jazbinšek, H.-J. Scheer, K. Kim, and M. Burghoff, "An advanced phantom study assessing the feasibility of neuronal current imaging by ultra-low-field NMR," *Journal of Magnetic Resonance*, vol. 237, pp. 182–190, 2013.

[20] M. S. Hämäläinen and R. J. Ilmoniemi, "Interpreting magnetic fields of the brain: minimum norm estimates," *Medical & Biological Engineering & Computing*, vol. 32, pp. 35–42, 1994.

[21] S. Supek and C. J. Aine, eds., *Magnetoencephalography: From Signals to Dynamic Cortical Networks*. Berlin/Heidelberg: Springer-Verlag, 2014.

[22] A. I. Ahonen, M. S. Hämäläinen, R. J. Ilmoniemi, M. J. Kajola, J. E. T. Knuutila, J. T. Simola, and V. A. Vilkman, "Sampling theory for neuromagnetic detector arrays," *IEEE Transactions on Biomedical Engineering*, vol. 40, no. 9, pp. 859–869, 1993.

[23] H. J. M. ter Brake, F. H. Fleuren, J. A. Ulfman, and F. J, "Elimination of flux-transformer crosstalk in multichannel SQUID magnetometers," *Cryogenics*, vol. 26, pp. 667–670, 1986.

[24] R. H. Koch, J. Z. Sun, V. Foglietti, and W. J. Gallagher, "Flux dam, a method to reduce extra low frequency noise when a superconducting magnetometer is exposed to a magnetic field," *Applied Physics Letters*, vol. 67, no. 5, pp. 709–711, 1995.

[25] J. Luomahaara, P. T. Vesanen, J. Penttilä, J. O. Nieminen, J. Dabek, J. Simola, M. Kiviranta, L. Grönberg, C. J. Zevenhoven, R. J. Ilmoniemi, and J. Hassel, "All-planar SQUIDs and pickup coils for combined MEG and MRI," *Superconductor Science and Technology*, vol. 24, p. 075020, 2011.

[26] A. Mäkinen, "Smart digital control of superconducting quantum interference devices for ultra-low-field magnetic resonance imaging," Master's Thesis, Aalto University, Finland, 2015.

[27] R. B. Scott, *Cryogenic Engineering*. New York: D. Van Nostrand Company Inc., 1959.

[28] G. K. White, *Experimental Techniques in Low-Temperature Physics*. Oxford: Calendron Press, 2006.

[29] Y. A. Çengel and A. J. Ghajar, *Heat and Mass Transfer: Fundamentals & Applications*. New York: McGraw-Hill, 4th ed., 2011.

[30] J. H. Lienhard IV and J. H. Lienhard V, *A Heat Transfer Textbook*. New York: Dover Publications Inc., 4th ed., 2011.

[31] R. Siegel and J. Howell, *Thermal Radiation Heat Transfer*. New York: Taylor & Francis, 4th ed., 2002.

[32] C. A. Bailey, ed., *Advanced Cryogenics*. London: Plenum Press, 4th ed., 1971.

[33] S. D. Augustynowicz and J. E. Fesmire, "Cryogenic insulation system for soft vacuum," *Advances in Cryogenic Engineering*, pp. 1691–1698, 2000.

[34] W. Stanley, "Heat-insulated receptacle." US Patent No. 1071817 A, 1912.

[35] W. D. Cornell, "Radiation shield supports in vacuum insulated containers." US Patent No. 2643022 A, 1953.

[36] E. M. W. Leung, R. W. Fast, H. L. Hart, and J. R. Heim, "Techniques for reducing radiation heat transfer between 77 K and 4.2 K," *Advances in Cryogenic Engineering*, pp. 489–499, 1980.

[37] Y. M. Eyssa and O. Okasha, "Thermodynamic optimization of thermal radiation shields for cryogenic apparatus," *Cryogenics*, vol. 18, no. 5, pp. 305–307, 1978.

[38] P. A. Augusto, T. Castelo-Grande, P. Augusto, and D. Barbosa, "Optimization of refrigerated shields using multilayer thermal insulation: Cryostats design – analytical solution," *Cryogenics*, vol. 46, no. 6, pp. 449–457, 2006.

[39] A. D. Caplin and A. T. Cayless, "Simple numerical modelling technique for cryostat design," *Cryogenics*, vol. 26, pp. 678–681, 1986.

[40] S. Taulu, J. Simola, J. Nenonen, and L. Parkkonen, "Novel Noise Reduction Methods," in *Magnetoencephalography: From Signals to Dynamic Cortical Networks* (S. Supek and C. J. Aine, eds.), pp. 35–71, Berlin/Heidelberg: Springer-Verlag, 2014.

[41] K. C. J. Zevenhoven and S. Alanko, "Ultra-low-noise amplifier for ultra-low-field MRI main field and gradients," in *Journal of Physics: Conference Series*, vol. 507, p. 042050, 2014.

[42] J. O. Nieminen, P. T. Vesanen, K. C. J. Zevenhoven, J. Dabek, J. Hassel, J. Luomahaara, J. S. Penttilä, and R. J. Ilmoniemi, "Avoiding eddy-current problems in ultra-low-field MRI with self-shielded polarizing coils," *Journal of Magnetic Resonance*, vol. 212, no. 1, pp. 154–160, 2011.

[43] K. C. J. Zevenhoven, H. Dong, R. J. Ilmoniemi, and J. Clarke, "Dynamical cancellation of pulse-induced transients in a metallic shielded room for ultra-low-field magnetic resonance imaging," *Applied Physics Letters*, vol. 106, p. 034101, 2015.

[44] J. Nenonen, J. Montonen, and T. Katila, "Thermal noise in biomagnetic measurements," *Review of Scientific Instruments*, vol. 67, no. 6, pp. 2397–2405, 1996.

[45] T. Varpula and T. Poutanen, "Magnetic field fluctuations arising from thermal motion of electric charge in conductors," *Journal of Applied Physics*, vol. 55, no. 11, pp. 4015–4021, 1984.

[46] J. B. Johnson, "Thermal agitation of electricity in conductors," *Nature*, vol. 119, pp. 50–51, 1927.

[47] J. B. Johnson, "Thermal agitation of electricity in conductors," *Physical Review*, vol. 32, pp. 97–109, 1928.

[48] H. Nyquist, "Thermal agitation of electric charge in conductors," *Physical Review*, vol. 32, no. 1928, pp. 110–113, 1928.

[49] D. T. Gillespie, "The mathematics of Brownian motion and Johnson noise," *American Journal of Physics*, vol. 64, no. 3, pp. 225–240, 1996.

[50] L. Vant-Hull, R. A. Simpkins, and J. T. Harding, "Disappearance of thermal magnetic fluctuations in a superconductor," *Physical Letters A*, vol. 24, no. 13, pp. 736–737, 1967.

[51] J. T. Harding and J. E. Zimmerman, "Quantum interference magnetometry and thermal noise from a conducting environment," *Physics Letters A*, vol. 27, no. 10, pp. 670–671, 1968.

[52] J. E. Zimmerman, "SQUID instruments and shielding for low-level magnetic measurements," *Journal of Applied Physics*, vol. 48, no. 2, pp. 702–710, 1977.

[53] J. A. Sidles, J. L. Garbini, W. M. Dougherty, and S.-H. Chao, "The classical and quantum theory of thermal magnetic noise, with applications in spintronics and quantum microscopy," *Proceedings of the IEEE*, vol. 91, no. 5, pp. 799–816, 2003.

[54] B. J. Roth, "Thermal fluctuations of the magnetic field over a thin conducting plate," *Journal of Applied Physics*, vol. 83, no. 2, pp. 635–638, 1998.

[55] H. Sandin, P. L. Volegov, M. A. Espy, A. N. Matlashov, I. M. Savukov, and L. J. Schultz, "Noise modeling from conductive shields using Kirchhoff equations," *IEEE Transactions on Applied Superconductivity*, vol. 21, no. 3, pp. 489–492, 2011.

[56] S.-K. Lee and M. V. Romalis, "Calculation of magnetic field noise from high-permeability magnetic shields and conducting objects with simple geometry," *Journal of Applied Physics*, vol. 103, no. 8, p. 084904, 2008.

[57] J. Nenonen, T. Katila, and J. Montonen, "Thermal noise of a biomagnetic measurement dewar," in *Advances in Biomagnetism* (S. J. Williamson, M. Hoke, G. Stroink, and M. Kotani, eds.), pp. 729–732, New York: Plenum, 1990.

[58] S. Hwang, K. K. Yu, Y. H. Lee, C. S. Kang, K. Kim, and S. J. Lee, "Analysis and reduction of thermal magnetic noise in liquid-He dewar for sensitive low-field nuclear magnetic resonance measurements," *Progress in Superconductivity and Cryogenics*, vol. 15, no. 2, pp. 20–23, 2013.

[59] H. C. Seton, J. M. S. Hutchison, and D. M. Bussell, "Liquid helium cryostat for SQUID-based MRI receivers," *Cryogenics*, vol. 45, no. 5, pp. 348–355, 2005.

[60] H. C. Seton, D. M. Bussell, J. M. S. Hutchison, and D. J. Lurie, "Use of a DC SQUID receiver preamplifier in a low field MRI system," *IEEE Transactions on Appiled Superconductivity*, vol. 5, no. 2, pp. 3218–3221, 1995.

[61] R. Mayrhofer, J. Stipsitz, R. Koerber, J. Stampfl, and P. Schoenhuber, "Structuring metallic coatings to reduce eddy currents and thermal noise in super insulation," *Journal of Physics: Conference Series*, vol. 507, p. 042025, 2014.

[62] R. McDermott, S. Lee, B. ten Haken, A. H. Trabesinger, A. Pines, and J. Clarke, "Microtesla MRI with a superconducting quantum interference device," *Proceedings of the National Academy of Sciences of the United States of America*, vol. 101, no. 21, pp. 7857–7861, 2004.

[63] I. Hilschenz, R. Körber, H.-J. Scheer, T. Fedele, H.-H. Albrecht, A. Mario Cassará, S. Hartwig, L. Trahms, J. Haase, and M. Burghoff, "Magnetic resonance imaging at frequencies below 1 kHz," *Magnetic Resonance Imaging*, vol. 31, pp. 171–177, 2013.

[64] B. Inglis, K. Buckenmaier, P. SanGiorgio, A. F. Pedersen, M. A. Nichols, and J. Clarke, "MRI of the human brain at 130 microtesla," *Proceedings of the National Academy of Sciences of the United States of America*, vol. 110, no. 48, pp. 19194–19201, 2013.

[65] V. Musilova, P. Hanzelka, T. Kralik, and A. Srnka, "Low temperature radiative properties of materials used in cryogenics," *Cryogenics*, vol. 45, no. 8, pp. 529–536, 2005.

[66] K. C. J. Zevenhoven, "Solving transient problems in ultra-low-field MRI," Master's Thesis, Aalto University, Finland, 2011.

[67] K. C. J. Zevenhoven, S. Busch, M. Hatridge, F. Öisjöen, R. J. Ilmoniemi, and J. Clarke, "Conductive shield for ultra-low-field magnetic resonance imaging: Theory and measurements of eddy currents," *Journal of Applied Physics*, vol. 115, no. 10, p. 103902, 2014.

[68] P. D. Desai, H. M. James, and C. Y. Ho, "Electrical resistivity of aluminum and manganese," *Journal of Physical and Chemical Reference Data*, vol. 13, no. 4, pp. 1131–1172, 1984.